

# Revealing recurrent regimes of mid-latitude atmospheric variability using novel machine learning method

Dmitry Mukhin,<sup>1</sup> Abdel Hannachi,<sup>2</sup> Tobias Braun,<sup>3</sup> and Norbert Marwan<sup>3</sup>

<sup>1</sup>*Institute of Applied Physics of the Russian Academy of Science, Nizhny Novgorod, Russia*

<sup>2</sup>*Department of Meteorology, Stockholm University, Stockholm, Sweden*

<sup>3</sup>*Potsdam Institute for Climate Impact Research, Potsdam, Germany*

(\*Dmitry Mukhin: mukhin@ipfran.ru)

(Dated: 1 February 2024)

The low frequency variability of the extratropical atmosphere involves hemispheric-scale recurring, often persistent, states known as teleconnection patterns or regimes, which can have profound impact on predictability on intra-seasonal and longer timescales. However, reliable data-driven identification and dynamical representation of such states are still challenging problems in modeling dynamics of the atmosphere. We present a new method, which allows both to detect recurring regimes of atmospheric variability, and to obtain dynamical variables serving as an embedding for these regimes. The method combines two approaches from nonlinear data analysis: partitioning a network of recurrent states with studying its properties by the recurrence quantification analysis and the kernel principal component analysis. We apply the method to study teleconnection patterns in a quasi-geostrophical model of atmospheric circulation over the extratropical hemisphere as well as to reanalysis data of geopotential height anomalies in the mid-latitudes of the Northern Hemisphere atmosphere in the winter seasons from 1981 to the present. It is shown that the detected regimes as well as the obtained set of dynamical variables explain large-scale weather patterns, which are associated, in particular, with severe winters over Eurasia and North America. The method presented opens prospects for improving empirical modeling and long-term forecasting of large-scale atmospheric circulation regimes.

**Behavior of weather systems over the mid-latitudes is well-known as strongly chaotic and having a very limited horizon of reliable forecasting. While movements of synoptic-scale structures like cyclones and anticyclones are predicted well within 1-2 weeks, larger structures of atmospheric circulation with longer time scales are still poorly investigated. As it is shown by models and data analysis, dynamics on these time scales, also called the low-frequency variability, is characterized by recurrent global patterns, or regimes, which can strongly impact long-term weather conditions in different regions. However, both identification and dynamical representation of such regimes based on data is a controversial problem due to the lack of robust and reliable methods of data analysis/data analysis methods. Here we suggest a method which allows to detect the regimes and, simultaneously, to obtain dynamical variables representing their dynamics. The method involves and joins together/combines several approaches from nonlinear data analysis: partitioning a network of recurrent states, recurrence quantification analysis and nonlinear principal component analysis. Studying winter low frequency variability (LFV) in the Northern Hemisphere mid-latitudes by the suggested method allows us to reveal and investigate dynamical properties of large-scale weather patterns, which are associated, in particular, with severe winters over Eurasia and North America. The results presented open prospects for improving data-driven modeling and long-term forecasting of large-scale atmosphere circulation regimes.**

## I. INTRODUCTION

Many non-linear multidimensional systems exhibit chaotic behavior with a continuum of time scales, are poorly predictable, and are generally difficult to distinguish from a random process. However, in the state space of the system there may be sets of states in which the system is found more often than others. Such intermittently recurrent states can have varying lifetimes (or persistence) and regularity of occurrence. Their study is important from a practical point of view, because in the space of observables they correspond to the most typical regimes of the system dynamics. However, both the identification and analysis of their dynamical properties based on the observations are still challenging, especially when the observations live in a high-dimensional space, such as our weather and climate system<sup>1</sup>.

Studies of atmospheric variability often distinguish between synoptic scales which embed day-to-day variability steered by baroclinic instability in the storm track region, and low-frequency variability with longer time scales. Compared to baroclinic processes, low-frequency variability is still not entirely well understood and is known to be challenging to model and predict<sup>2</sup>. Low-frequency variability embeds, in particular, tropospheric planetary waves and coherent large-scale structures including blocking and different phases of teleconnections, such as the North Atlantic Oscillation (NAO). A proper understanding of low-frequency variability proves invaluable in improving weather/climate prediction on intraseasonal and/or seasonal timescales, in addition to many other applications not least subgrid parametrization, climate change feedback, downscaling etc, see, e.g., the review 3 and references therein.

The atmospheric system is a highly nonlinear dynamical

cal system with complex interactions between very many degrees-of-freedom involving different temporal and spatial scales. As far as large scale flow is concerned there is evidence of the existence of preferred recurrent and persistent circulation patterns<sup>3</sup>. For example, it is well known that northern hemisphere (NH) low-frequency variability is partly manifested by several teleconnection patterns<sup>4–8</sup>, which can have profound impact in improving predictability on intra-seasonal and longer, such as subseasonal to seasonal timescales<sup>9</sup>.

Compared to the tropics, extratropical dynamics involves a great variety of wave-wave and wave-mean flow interactions, highlighting, hence, more involved nonlinearity, in particular, preferred intra-seasonal large scale structures of nonlinear flow regimes. The persistence timescale of these patterns is normally much longer than synoptic baroclinic timescales but smaller than typical intra-seasonal variability timescales of radiative fluxes and bottom boundary conditions, such as sea surface temperature anomalies<sup>5,10,11</sup>.

The extratropical persistent and quasi-stationary states are associated with teleconnection patterns and states/positions of the jet stream<sup>12,13</sup>. An extensive number of studies has analysed and identified these nonlinear flow regimes ranging from various cluster analysis methods, bump hunting of the probability density function (pdf) to hidden Markov models and self-organizing maps. The number of these structures, however, is a matter of debate between researchers, and depends on the location and extension of the geographical region and season. An extensive discussion with more details can be found in the review 3, and references therein.

One of the challenging issues in the identification of the above extratropical nonlinear structures is the choice of the low-dimensional space, which allows appropriate reduction of weather-related noise and efficient separation of these states. The space spanned by the leading empirical orthogonal functions (EOF) is conventionally used as reduced space. EOFs have, however, a number of weaknesses putting limits on what can be achieved<sup>14,15</sup>. To overcome those weaknesses and, in consistency with the nonlinear nature of the dynamics, these authors applied kernel EOFs as a low-order state space to identify the nonlinear flow structures. In particular, those structures are interpreted as quasi-stationary states based on the flow tendency within the same space. This flow tendency can only be applied with very long time series, as is possible with the quasi-geostrophic model of potential vorticity on the sphere but is not appropriate for data from reanalysis.

Many problems in the real world, such as physical, computer, and social sciences, can be formulated and solved using the concept of networks or graph theory. A network is a collection of objects or nodes that are connected by edges. These connections can be defined based on a chosen metric in the system state space<sup>16</sup>. An example of such graphs can be found in the Isomap method<sup>17</sup> and an application to the Asian monsoon can be found in<sup>18</sup>. Many networks allow a natural splitting of the system into groups or communities/modules<sup>19</sup>. To complement the analysis of the low frequency variability system within the low-dimensional kernel EOF space, we adopt and apply here for the first time the concept of network modularity to study the nonlinear dynamical feature of the mid-

latitude atmosphere.

In this manuscript we revisit and extend the analysis of Hannachi and Iqbal<sup>14</sup> by using kernel EOFs combined with a recurrence network partitioning method<sup>19,20</sup>. The recurrence network analysis allows an elegant and easy partitioning of the state space into communities in a natural way, providing an efficient way to identify the nonlinear flow structure within the low-dimensional kernel EOF space. Moreover, this makes it possible to use the tools of recurrence quantification analysis (RQA)<sup>21</sup> to study important dynamical features of the detected structures.

The manuscript is organised as follows. Sect. II describes the methodology, the data and calculation procedure are given in Sect. 3, Sect. 4 presents the results, and a summary and conclusion are provided in the last section.

## II. METHODS

### A. Kernel principal component analysis

Detecting the regimes of a given (dynamical) system's variability can be formulated as the problem of separating structures of related states in the phase space. Typically, when studying the atmospheric dynamics, we have at our disposal multivariate time series of some physical variables, such as temperature, pressure, geopotential height, etc., on a spatial grid,  $\mathbf{x}_t, t = 1, \dots, N$ , and hence, the structures of interest are embedded in a high-dimensional space. The nonlinearity of the system makes traditional linear data decomposition methods, such as empirical orthogonal function (EOF) analysis, inefficient and sometimes inadequate in disentangling these structures. The reason is that they are not necessarily oriented along linear directions, but are possibly lying on complex manifolds, and may be embedded in a very large number of principal components (PCs). A suitable approach to overcome this complexity is to construct a nonlinear embedding of the state space, through a high-dimensional multivariate mapping  $\varphi(\cdot)$ , from the original state space into a new *feature* space, so that the structures would be captured and could be well-separated by a few PCs in the new feature space. In this setting, the problem is reduced to linear PCA applied to the transformed time series  $\varphi(\mathbf{x}_t)$  of the original multivariate  $d$ -dimensional time series  $\mathbf{x}_t$  with  $t = 1, \dots, N$ . A straightforward way to solve this problem – via explicit assignment of the functions  $\varphi$  – is in most cases impractical, because it is difficult to guess both the functional form and its dimension, which are optimal for detecting the regimes. The *kernel trick* can solve this problem in an elegant way. The kernel function  $K(\cdot, \cdot)$  can be defined as a scalar product in such a way that  $K(\mathbf{x}, \mathbf{y}) = \varphi(\mathbf{x})^T \varphi(\mathbf{y})$ , and can be chosen from a large family such as polynomials or Gaussian functions. The choice of  $K(\cdot, \cdot)$  then defines implicitly the mapping  $\varphi$ , i.e., without an explicit expression of it, which is generally very high (and may be even infinite) dimensional. Then, all we need to know for calculating PCs in the new feature space is the matrix of inner products  $K_{ij} = \varphi(\mathbf{x}_i)^T \varphi(\mathbf{x}_j) := \sum_l \varphi_l(\mathbf{x}_i) \varphi_l(\mathbf{x}_j)$ .

Hence specifying the mapping  $\varphi(\cdot)$  is not needed to perform PCA; we can just introduce the kernel function  $K(\cdot, \cdot)$  that defines the dot products  $K_{ij} = K(\mathbf{x}_i, \mathbf{x}_j)$ ,  $i, j = 1, \dots, N$ . Such an implicit kernel-based nonlinear transformation of the original space is the core idea of the kernel PCA (KPCA) approach<sup>1,22,23</sup>, which was shown to be effective, e.g., in identifying the LFV regimes in the extratropical atmosphere<sup>15</sup>. The kernel function can be selected based on some general assumptions reflecting the similarity of states within the state space. According to the spectral decomposition theorem, the kernel function may be decomposed into an infinite series as  $K(\mathbf{x}, \mathbf{y}) = \sum_l \lambda_l f_l(\mathbf{x}) f_l(\mathbf{y})$ , where  $f_l(\cdot)$ ,  $l = 1, 2, \dots$ , are the eigenfunctions of the integral operator with kernel  $K(\cdot, \cdot)$ . Accordingly, the mapping  $\varphi_l(\cdot)$ ,  $l = 1, 2, \dots$ , are then given by  $\varphi_l(\mathbf{x}) := \sqrt{\lambda_l} f_l(\mathbf{x})$ , as mentioned in Ref. 15. Thus, the approach makes it possible to consider infinite-dimensional embedding to achieve optimal separation of distinct states. Technically, in kernel PCA, the  $N \times N$  matrix  $\mathbf{K}$  is decomposed as follows

$$\mathbf{K} = \bar{\mathbf{K}} + \mathbf{K}_c = \bar{\mathbf{K}} + \sum_{i=1}^{N-1} \mathbf{u}_i \cdot \mathbf{u}_i^T. \quad (1)$$

where the mutually orthogonal vectors  $\mathbf{u}_i$ ,  $i = 1, \dots, N-1$ , are the kernel principal components (KPCs), and  $\bar{\mathbf{K}}$  is

$$\bar{\mathbf{K}} = \mathbf{K} - \mathbf{K}_c = \frac{1}{N}(\mathbf{1} \cdot \mathbf{K} + \mathbf{K} \cdot \mathbf{1}) - \frac{1}{N^2} \mathbf{1} \cdot \mathbf{K} \cdot \mathbf{1}, \quad (2)$$

representing the deviation of  $\mathbf{K}$  from the centered matrix  $\mathbf{K}_c = \mathbf{C} \cdot \mathbf{K} \cdot \mathbf{C}$ , with  $\mathbf{C}$  being the  $N \times N$  centering matrix  $\mathbf{C} = \mathbf{I} - \frac{1}{N} \mathbf{1}$ , and  $\mathbf{I}$  and  $\mathbf{1}$  are respectively the identity matrix and the matrix of the same size filled with ones. The centering of the kernel matrix excludes the temporal mean of the features (or states) in the feature space from the decomposition, which could result in a distortion of the decomposition as the leading KPC gets attracted towards the main diagonal. This allows us to treat  $\mathbf{K}_c$  as the matrix of covariances between the states at different times (temporal covariances) yielding, in particular, zero-mean of the KPCs. Thus, the KPC vectors  $\mathbf{u}_i$ ,  $i = 1, \dots, N-1$ , can be obtained from the eigendecomposition of the centered array  $\mathbf{K}_c$ :

$$\begin{aligned} \mathbf{K}_c &= \mathbf{V} \cdot \mathbf{D} \cdot \mathbf{V}^T, \\ \mathbf{u}_i &= D_{ii}^{1/2} \mathbf{v}_i, i = 1, \dots, N-1 \end{aligned} \quad (3)$$

where  $\mathbf{v}_i$  is the  $i^{\text{th}}$  eigenvector, forming the matrix  $\mathbf{V}$ , and  $D_{ii}$  is the corresponding eigenvalue – the variance of the  $i^{\text{th}}$  KPC.

Following the work 15, here we use kernels that are Gaussian function of a distance  $d(\cdot, \cdot)$  between state vectors at different times, i.e.,

$$K_{ij} = K(\mathbf{x}_i, \mathbf{x}_j) = \exp(-d^2(\mathbf{x}_i, \mathbf{x}_j)/2\sigma^2). \quad (4)$$

Such a distance-based Gaussian kernel accounts for local similarity between the states, which is a useful property for capturing nonlinear manifolds in the phase space. The only generalization allowed in Eq.(4), compared to the kernels used in

Ref. 15, is the use of an arbitrary metric (not necessarily Euclidean) determined by the specific problem. However, using some metric  $d(\cdot, \cdot)$ , we should ensure that the kernel function Eq.(4), and, hence, the matrix  $\mathbf{K}$ , are positive semi definite, since they are designed to define an inner product. This requirement is fulfilled with those metrics for which the metric space can be embedded in the Euclidean space<sup>24</sup>. In case of other metrics, when negative eigenvalues of the kernel matrix are possible<sup>25</sup>, we may consider using an *approximation* of  $\mathbf{K}$  by a positive semi definite matrix instead.

By applying KPCA to multidimensional time series we can expect clustering of the states in a space with low- to moderate number of KPCs, so that each cluster can be associated with certain circulation regime of variability. The problem here is that neither the number of clusters, nor the dimension of the subspace in which the clusters are embedded, are *a priori* known. This means that these parameters should be optimized for obtaining statistically justified clustering. However, reliable optimization of the clustering procedure is difficult in real climate applications, due to insufficient statistics from the limited observed time series. Moreover, the clusters can have substantially non-Gaussian shapes, thus making such robust methods as, e.g., Gaussian mixture models<sup>26</sup> or kernel density estimate<sup>27</sup>, inefficient. Below we describe a method providing the detection of significant regimes that avoids such difficulties.

## B. Recurrence network partitioning

Conventional recurrence networks are based on neighborhood thresholding using a Euclidean metric between pairs of states<sup>16</sup>. Given a set of multivariate states  $\mathbf{x}_t$ ,  $t = 1, \dots, N$ , and a recurrence threshold  $\varepsilon$ , the recurrence matrix  $\mathbf{R} = (R_{ij})$  is defined by  $R_{ij} = 1_{\|\mathbf{x}_i - \mathbf{x}_j\| < \varepsilon}$ , that is 1 if  $\|\mathbf{x}_i - \mathbf{x}_j\| < \varepsilon$ , and zero otherwise<sup>21</sup>. In this regard the kernel matrix  $\mathbf{K}$  can be used to produce a recurrence matrix through binarization using the metric  $d(\cdot, \cdot)$  and threshold  $\gamma$  as:

$$R_{ij}(\gamma) = \begin{cases} 1, & K(\mathbf{x}_i, \mathbf{x}_j) > \gamma \\ 0, & \text{otherwise.} \end{cases} \quad (5)$$

This matrix can be visualized as a recurrence plot (RP), by plotting  $R_{ij} = 1$  as a black pixel (and blank elsewhere). A line is then defined as a sequence of successive black pixels. A recurrence network is a graph using  $\mathbf{R}$  as the adjacency matrix. The nodes of the graph correspond to the observed states  $\mathbf{x}_t$ , and if two states  $\mathbf{x}_i$  and  $\mathbf{x}_j$  are neighbors with respect to the metric  $d(\cdot, \cdot)$ , then the corresponding nodes are connected by an edge, i.e.,  $R_{ij} = 1$ . The number  $k_i = \sum_{j=1}^N R_{ij}$  is the degree of node  $i$  and represents the number of nodes connected to it (i.e., the number of recurrences of the state at time  $i$ ). With this conceptual framework, the problem of regime detection can be formulated as recognizing communities of nodes, such that there are significantly more connections within communities than between them – a situation akin to  $k$ -means clustering concerning between- and within-variances. Actually, each community joins the related states of the system based on the

similarity measure Eq.(4). Therefore, dividing the network into communities allows matching each state to a certain type of behavior.

To detect the communities we use an approach suggested by Newman<sup>28</sup>, in which the best division of the network maximizes a special cost-function called modularity. For a given division, the modularity measures the difference between the fraction of edges falling within the communities and the same fraction expected from a network with randomly distributed connections, regardless of the division. This random network is assumed to have the same number and degrees of nodes as in the analyzed network. Since elements of the matrix  $R$  can only take 0 or 1, the expected value of  $R_{ij}$  in a network with random connections equals to the probability to find an edge between nodes  $i$  and  $j$ . This probability is estimated as  $k_i k_j / 2m$ , where  $m = \frac{1}{2} \sum_{i=1}^N k_i$ , and represents the total number of edges in the network. The modularity is then expressed as

$$Q = \frac{1}{2m} \sum_{i,j} \left( R_{ij} - \frac{k_i k_j}{2m} \right) g_{ij} = \frac{1}{2m} \sum_{i,j} \bar{R}_{ij} g_{ij}, \quad (6)$$

with  $g_{ij} = 1$  if nodes  $i$  and  $j$  belong to the same community and 0 otherwise. Here the matrix  $\bar{R}_{ij}$  represents the deviation of  $R$  from the expected adjacency matrix of a random network.

An elegant way to find the communities maximizing Eq. (6) was proposed in Ref. 19. The approach is based on iteratively splitting each community into two communities so that each split must provide the maximal positive increment of the whole network modularity, until indivisible communities are obtained. Let us consider a particular community  $\mathbf{H}$  – a subset of nodes of our network – which we wish to split. If we are, for example, at the starting point of the algorithm, then  $\mathbf{H}$  is the whole set of nodes indexed by  $i = 1, \dots, N$ . Splitting  $\mathbf{H}$  into two groups can be represented by a vector  $\mathbf{s}$  (classifier or indicator), whose elements  $s_i = -1$  for the first group and  $s_i = 1$  for the second. Note that the dimension of  $\mathbf{s}$  is the size  $i_H$  of  $\mathbf{H}$ . It can be shown that the increment  $\Delta Q$  of the whole network modularity, after this split, takes the form:

$$\Delta Q = \frac{1}{4m} \mathbf{s}^T \mathbf{B} \mathbf{s} = \frac{1}{4m} \mathbf{s}^T \mathbf{W} \Theta \mathbf{W}^T \mathbf{s}, \quad (7)$$

$$\mathbf{B} = (B_{ij}), \text{ with } B_{ij} = \bar{R}_{ij}^{(H)} - \delta_{ij} \sum_{k \in \mathbf{H}} \bar{R}_{ik}^{(H)},$$

where  $\bar{\mathbf{R}}^{(H)}$  is the submatrix of  $\bar{\mathbf{R}} = (\bar{R}_{ij})$  obtained by selecting the elements of  $\bar{\mathbf{R}}$  with the indices  $i, j \in \mathbf{H}$ ,  $\delta_{ij}$  is the Kronecker delta, and  $\mathbf{W} \Theta \mathbf{W}^T$  is the eigendecomposition of the matrix  $\mathbf{B}$ , with  $\Theta = \text{diag}(\theta_0, \dots, \theta_{i_H-1})$ . Accordingly, the problem of splitting  $\mathbf{H}$  boils down to finding the classifier (or indicator) vector  $\mathbf{s}$  consisting of numbers 1 and  $-1$  that maximizes the quadratic form, Eq. (7), which is equivalent to maximizing the dot product of  $\mathbf{s}$  with the eigenvector  $\mathbf{w}_0$  of the matrix  $\mathbf{B}$  corresponding to its largest eigenvalue  $\theta_0$ . The exact solution is the vector  $\mathbf{s}$  with components  $s_i$  having the same sign as the corresponding components  $w_{0i}$  of the leading eigenvector  $\mathbf{w}_0$  of  $\mathbf{B}$ . If the matrix  $\mathbf{B}$  has positive eigenvalues, two new communities defined by the vector  $\mathbf{s}$  will emerge, provided

that  $\Delta Q > 0$ . Otherwise, if there are no positive eigenvalues in  $\mathbf{B}$ , its largest eigenvalue is always zero, since one of the properties of this matrix is the zero sum over each row or column. In this case, all components of the leading eigenvector have the same value, which means that all  $s_i$  are also the same, i.e.  $\mathbf{H}$  is no longer divisible. The described splitting process of the network communities can continue until the  $\Delta Q > 0$  condition is violated for each current community<sup>29</sup>.

Besides the indicator or classifier vector  $\mathbf{s}$ , useful information about the structure of the resulting communities is also provided by the leading eigenvector  $\mathbf{w}_0$ . As it can be seen from Eq.(7), the absolute value of  $w_{0i}$  measures the contribution of the  $i^{\text{th}}$  element to the modularity of the network, i.e., the gain in modularity from the inclusion of the corresponding node in the community. The number  $|w_{0i}|$  is referred to as the *centrality* of the corresponding node in the resulting community, and therefore for each community we get a vector of centralities. In terms of interpretation in connection to the atmospheric circulation regime detection, large centrality of some node  $k$  of the network indicates that the corresponding spatial pattern  $\mathbf{x}_k$  is similar to a large number of other patterns belonging to the same community, and represents therefore a typical pattern for the regime associated with this community.

The main advantage of Newman's method described above is that it provides an efficient and elegant way to cluster the network into communities without any prior information on their size and number using simple matrix calculations. This is particularly convenient in climate data analysis where the set of regimes is not known in advance and the problem of the data-driven identification comes to the forefront. The suggested method of decomposing the analyzed time series allows us to label the states of the system in the space of the leading kernel PCs in accordance with the detected communities. As a result, looking at the labelled/marked states in the KPC space, we can easily select a number of leading KPCs that provides clear separation of the communities (see the results below and a simple example in Appendix). Further, the selected KPCs can play the role of dynamical variables that describe the sporadic switching of the system trajectory between the dynamical circulation regimes.

### C. Studying dynamical properties of the regimes

The adjacency (recurrence) matrices of the partitioned recurrence networks can be analysed using RQA<sup>21</sup>. Each regime-specific recurrence plot (RP) can be regarded as a particular subset of the full RP constrained by the community labels. In order to compare the dynamical properties of the different regimes, RQA is carried out separately for each regime-specific RP.

A simple quantifier for the overall intrinsic *similarity* of an atmospheric regime can be defined by the ratio of total recurrences in the regime-specific RP relative to the (squared) time that is spent in the respective regime, i.e., recurrence rate RR,  $RR = \sum_{i,j} R_{ij} / N^2$ . In traditional RQA, the statistics of diagonal and vertical line structures are studied to characterize the predictability and intermittency of a system. Diagonal lines

in an RP reflect time periods during which two segments of the phase space trajectory evolve in parallel, indicating deterministic and well-predictable dynamics. By counting the number of diagonal lines that exceed a specific length for the regime-specific RPs, we study if the evolution of spatial patterns during different time periods is similar. *Predictability* of atmospheric patterns in each regime is quantified by the determinism DET of the RP which is given as the fraction of diagonal lines that exceed a minimum line length of  $l_{\min} = 5$  days to all diagonal lines, i.e.  $DET = \sum_{l \geq l_{\min}} lP(l) / \sum lP(l)$ , where  $P(l)$  is the distribution of diagonal line lengths  $l$ . Vertical lines in an RP identify periods in which the dynamics are ‘slowed down’. Consequently, we interpret them as corresponding to quasi-stationary patterns potentially associated with atmospheric blocking and possibly zonal flow. *Persistence* of atmospheric patterns in each regime is quantified by laminarity LAM which is computed as the fraction of the total vertical lines with  $l_{\min} = 5$  days to all vertical lines:  $LAM = \sum_{v \geq v_{\min}} vP(v) / \sum vP(v)$ , where  $P(v)$  is the distribution of vertical line lengths  $v$ . Recently, an approach using recurrence lacunarity (RL) was proposed to characterize features of an RP that are distributed among multiple time scales and are not necessarily expressed in line structures<sup>30</sup>. RL generally reflects the heterogeneity of an RP. Thus, we interpret it as the *diversity* of the regime behavior. While regular RL informs about the general heterogeneity of recurrences, its extension to diagonal/vertical line structures is straight-forward and is introduced here. For the computation of diagonal/vertical line RL (dRRL/vRRL), the number of diagonal/vertical lines exceeding  $l_{\min} = 5$  days in each box is counted and reflects how strongly predictability/persistence of atmospheric patterns varies throughout different time periods. The box width is fixed to one year, highlighting interannual variability. High values indicate that, e.g., high persistence during one time period only has limited implications for other time periods. Thus, we always show these three different RL-based measures of diversity.

Significance testing allows to test the dynamical properties of atmospheric regimes against different null hypotheses. We test for two different hypothesis: (i) we check whether the recurrence network partitioning yields regimes that are significantly different from random regimes with respect to above mentioned recurrence quantifiers and (ii) we test which regime yields significantly high values for a given recurrence quantifier.

The first test is done by random deletion of recurrences from the full RP. In particular, for the  $i^{\text{th}}$  regime-specific RP with  $n_i$  recurrences, we randomly delete  $m = N - n_i$  recurrences from the full RP that contains  $N > n_i$  recurrences while also reproducing the column-wise recurrence rate of the  $i^{\text{th}}$  regime-specific RP. We generate 200 random samples for each RP and compute the 99%-quantile for each RQA measure from this ensemble as an upper confidence level to test for significance.

For the second test, we apply a bootstrapping procedure with  $n_B = 2,000$  runs<sup>31</sup>: we first collect all diagonal lines(/vertical lines/counts) from the distributions obtained from each regime-specific RP separately. In a single bootstrap

run, we draw  $M$  times (with replacement) from the unification of these length(/count) distributions and compute the measure of interest, yielding a single value.  $M$  is given by the number of lines/the total count in the  $i^{\text{th}}$  regime-specific RP. By repeating this procedure  $n_B$  times, an empirical test distribution for this measure is obtained from which we compute the upper 99%-confidence level. This method is applied for all measures except the recurrence rate; in this case, we test against the hypothesis that recurrences are distributed among the regimes with respect to the time spent in each regime. Consequently, we obtain each regime-specific significance level by dividing the total number of recurrences (from all regimes) by the individual (squared) time spent in a regime.

#### D. Method summary

The whole procedure described in the above subsections A-C is represented schematically in Fig. 1. The main goal of the KPCA is to obtain a few number of variables (leading KPCs) which are suitable for differentiating the obtained regimes. The same kernel matrix as in KPCA is used for building the recurrence network which partitioning yields a set of regimes. As a result, we obtain a state space in which the regimes are well separated as well as representation of the regimes in physical space via composites, and can study properties of the regimes by the RQA methodology.

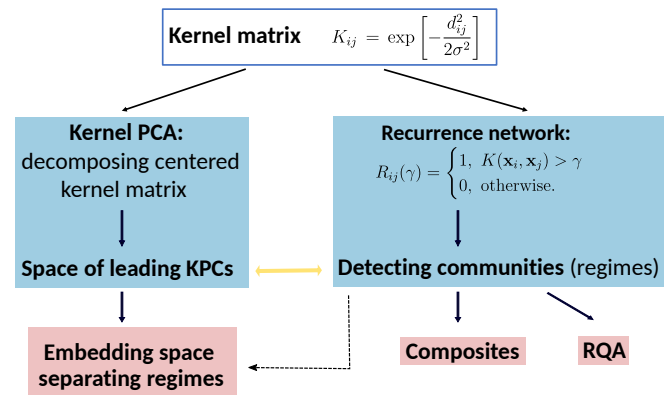


FIG. 1: Schematic representation of the proposed procedure.

### III. DATA AND CALCULATION SETUP

#### A. QG3 model time series

Quasi-geostrophic (QG) models of the atmosphere are popular polygons for testing algorithms concerning weather/climate dynamics. Being simplified representations of atmospheric dynamics, QG models demonstrate a rich spectrum of variability at different time scales and are competitive to intermediate and full general circulation models regarding complexity and dynamical features/processes. Here we use time series generated by a three-level QG model

(QG3) on the sphere<sup>32</sup> with realistic orography and surface boundary condition. Based on the potential vorticity equations at three (200, 500, and 800 hPa) pressure levels<sup>32–34</sup>, the model is tuned to simulate winter atmospheric circulation over the extratropical hemisphere. The model exhibits highly nonlinear behavior with a chaotic attractor in its phase space with more than 100 positive Lyapunov exponents<sup>33</sup>. The LFV behaviour of the model regimes was studied in a number of works, based on different kinds of clustering in a truncated phase space. In particular, the authors of the work 35 identified four clusters in the space of three leading PCs calculated from a very long (54,000 days) time series of the mid-level stream function anomalies (SFA). These clusters are associated with the well-documented atmospheric modes or teleconnections, namely, Arctic oscillations (AO) and North Atlantic oscillation (NAO). Similar results were obtained in Ref. 36 based on reduced data-driven models, but using a much shorter sample of 5,000 days. Hannachi and Iqbal<sup>15</sup> used KPCs as a space for a PDF-based cluster detection; however, only two clusters related to the AO were detected. Here we present results of our analysis applied to three 10,000-day time series of the mid-level stream function anomalies, distributed over latitudes 36°N to 90°N with approximately  $5.5 \times 5.5$  degree resolution. These non-overlapping time series are randomly taken from a very long (300,000 days) QG3-model run. Then the analysis is performed to each time series independently.

## B. Reanalysis data

To study the circulation regimes of the real atmosphere, we use daily geopotential height (HGT) time series at the 500 hPa pressure level from the NCEP/NCAR reanalysis dataset<sup>37</sup>. The time series is provided on a  $2.5 \times 2.5$  degree latitude-longitude resolution, north of 30°N covering the period 1980 to 2020. The data are de-seasonalized by removing the daily seasonal mean signal over the whole period smoothed in time with a Gaussian window with the standard deviation of 15 days. Such smoothing suppresses the day-to-day noise in the resulting annual cycle, while re-retain the intra-annual seasonal structure. Only winter (December-January-February) values are taken from the obtained time series of daily HGT anomalies, yielding a sample of 3,579 days.

## C. Distance metric, kernel and recurrence matrices

Since our goal is to separate sets of states, each of which joins spatial patterns yielding similar atmospheric conditions, we focus on the pattern's structure/shape rather than their amplitudes. Accordingly, we define a distance given by the sine of the angle  $\alpha_{ij}$  between pairs of patterns:

$$d(\mathbf{x}_i, \mathbf{x}_j) = \left\| \frac{\mathbf{x}_i}{\|\mathbf{x}_i\|} - \frac{\mathbf{x}_j}{\|\mathbf{x}_j\|} \right\| = 2 \left| \sin \frac{\alpha_{ij}}{2} \right|, \quad (8)$$

where  $\|\mathbf{x}\| = (\mathbf{x}^T \Lambda \mathbf{x})^{\frac{1}{2}}$  is the metric using a  $d \times d$  diagonal weighting matrix  $\Lambda$  reflecting the non-uniformity of the spatial

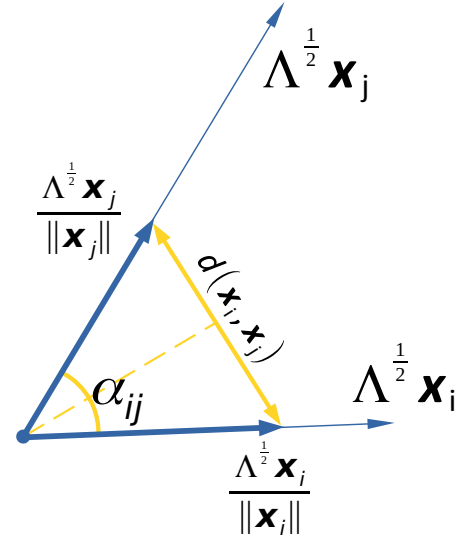


FIG. 2: Representation of the distance defined by Eq. 8.

grid (see below). Clearly, this metric inherits all properties of the Euclidean metric, as it is nothing more than the Euclidean distance between the weighted vectors  $\Lambda^{\frac{1}{2}} \mathbf{x}$  normalized to unit norm (see Fig. 2). This always yields a positive semi-definite kernel matrix Eq. (4).

A very important parameter that determines the recurrence network structure and strongly impacts the splitting of the network into communities is the threshold  $\gamma$  in the definition of the recurrence matrix, Eq. (5)<sup>38</sup>. If it is too large (remember that here the thresholding is opposite to the classical recurrence definition), the network degenerates into many communities yielding high modularity. Such a network may eventually not help to reveal any connections between patterns except those close in time. If, on the contrary,  $\gamma$  is too small,

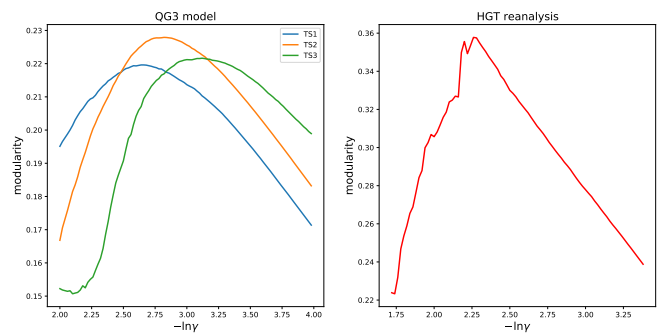


FIG. 3: Modularity increment after first division of the network into two communities vs. the threshold  $\gamma$ . Curves obtained from the three time series of the QG3 model and the HGT reanalysis time series are plotted in the left and right panels, respectively.

we end up with a poorly divisible network, in which each node is connected to most of the remaining nodes. Hence, this calls for the need to optimize the threshold parameter. Here



we select  $\gamma$  to provide the best division of the network into two basic communities at the initial splitting of the whole network. Under this requirement, the resulting value of  $\gamma$  maximizes the modularity increment  $\Delta Q(\gamma)$  at the first iteration of the algorithm. Such a choice is justified in the case of mid-latitude atmospheric dynamics, since two opposite types of circulation associated with the strength of the polar vortex are known to be the dominant modes in this region<sup>39</sup>, and the network should distinguish them well at the most basic level. It is obtained (see Fig. 3) that there are pronounced maxima of this dependence for both datasets considered here. By adjusting  $\gamma$  we do not need to care too much about the precise value of  $\sigma$  in the kernel function, Eq. (4). We find that setting  $\sigma = 2 \min_{i,j} d(\mathbf{x}_i, \mathbf{x}_j)$  in all examples below provides quite robust results, which is close to assumptions from the work 15.

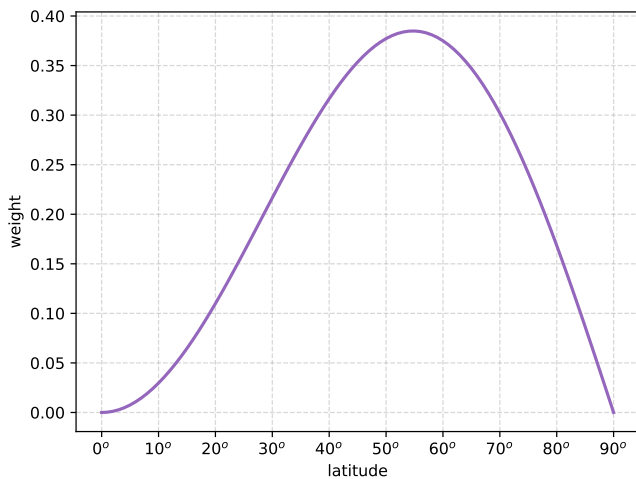


FIG. 4: Dependence of the weight given by Eq. (9) on latitude.

#### D. Data weighting

The data considered here is defined on a grid that is uniform in polar coordinates, so its cells cover unequal areas. In line with the traditional approach, we had to distribute the weights of the grid nodes in the distances  $d(\mathbf{x}_i, \mathbf{x}_j)$ , Eq.(8), according to the area fractions around each grid node. This corresponds to weights  $\Lambda_{mm} \propto \cos \theta_m$ , where  $\theta_m$  is the latitude (in radians) of the  $m^{\text{th}}$  component  $x_m$  (or  $m^{\text{th}}$  grid point)  $m = 1, \dots, d$ , of the state vector  $\mathbf{x}$ . A main problem with such weighting in our case is related to the resulting larger magnitude of anomalies at the southern bound of the considered latitude band. This moves the focus of analysis from the mid-latitudes – the region of interest – to the subtropics. No weighting, on the other hand, yields dramatic increase of polar latitudes contribution, thus shifting focus on the Polar vortex region rather than the mid-latitude circulation. The problem of proper weighting was stated, e.g., in the works 40 and 41. Here, we take into account the latitudinal dependence of the

characteristic spatial scale of atmospheric anomalies responsible for planetary-scale circulation regimes. In the extratropics, this scale is proportional to the Rossby deformation radius<sup>42</sup>, which depends on the latitude as  $\frac{1}{\sin \theta}$ . Therefore, normalization of the grid cell areas through scaling by the characteristic areas of anomalies ( $\propto \frac{1}{\sin^2 \theta}$ ) allows us to better capture the peculiarities and typical features of the atmospheric circulation using a given spatial grid. As a result, we use weights in the distance measure that focus on the midlatitudes expressed as

$$\Lambda_{mm} = \cos \theta_m \sin^2 \theta_m, \quad (9)$$

or, equivalently, multiply the signal at each grid point by  $\sin \theta_m \sqrt{\cos \theta_m}$ . Such weighting distinguishes mid-latitudinal and subpolar nodes of the grid, reaching the maximum at approximately 55°N (Fig. 4).

## IV. RESULTS

### A. QG3 model time series

We apply the methodology described above to each of the three SFA time series separately. For all time series the recurrence network division method gives the same number of communities, or regimes, equal to three. To illustrate clustering of the communities in the KPC-space, we plot elements of each community in the plane of the two leading KPCs (see Fig. 5). The most typical (i.e., having large centralities in their communities) states from different communities are well-separated in this plane, and hence, these two variables can serve well as an embedding for the three identified regimes.

Unlike in EOF decomposition or some of its nonlinear generalizations (see, e.g., Refs. 43 and 44), there is no explicit mapping of the KPCs to the data space. A coarse geographical structure of SFA relating to a specified regime can be obtained via composite analysis, i.e., the spatial field of SFA averaged over the most central states of the regime (as shown in Fig. 5, top). The resulting composites are clearly related to the three well-known atmospheric teleconnection patterns (Fig. 6). The first two are the positive and negative phases of AO, connected with an anomalous pressure difference between the polar region and the mid-latitude belt, and, respectively, stronger or weaker (zonal) westerly flow. The third one resembles the negative Pacific North American (PNA) pattern characterized in winter seasons by dominating tripole structure with positive anomalies over the North Pacific and near southeastern United States and negative anomalies over central Canada. We note that we have not obtained a separate regime corresponding to NAO, but NAO-related anomalies are captured by mode 1, which encompasses the negative NAO phase, whereas modes 2 and 3 feature of the positive NAO phase.

Studying the nature of, and the relation between the various teleconnection patterns, including PNA, NAO and AO/NAM (Northern Hemisphere Annular Mode), has a long history (e.g. Refs. 4 and 5). The nonlinearity and/or non-distinguishability between the NAO and AO teleconnection

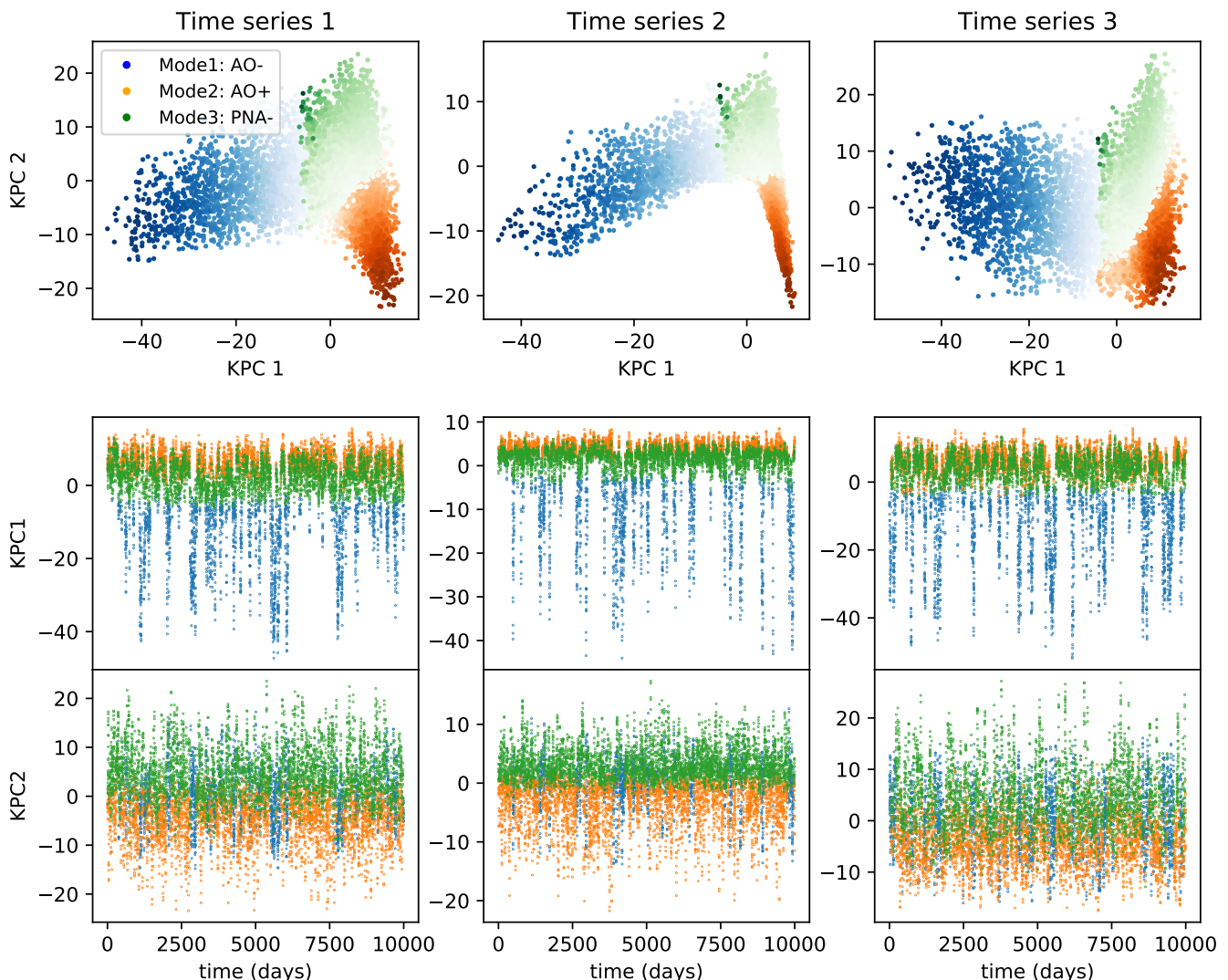


FIG. 5: Regimes of the QG3 model behavior in the space of the leading two KPCs. The three columns correspond to the three analyzed time series. In upper panels states of each regime (mode) are shown in the KPC1-KPC2 plane (see the text). States belonging to different regimes are marked by different colors; color saturation corresponds to the centrality of a state in its community. Time series of the KPC1 and KPC2 variables are plotted in the lower panels.

has been discussed thoroughly in the literature (e.g. Refs. 39 and 45). The linear EOF analysis, and even nonlinear cluster analysis cannot categorically distinguish between NAO and AO. For example, Feldestein and Franzke<sup>46</sup> examined, based on composite analysis the null hypothesis that the NAO and AO/NAM persistent events are not distinguishable. They found that the null hypothesis cannot be rejected even at 20% significance level. In another analysis, Dai and Tan<sup>47</sup> examined the nature of AO through SOM (Self Organizing Map) analysis. They found that AO, derived from the 250-hPa geopotential height anomalies, can be interpreted in terms of a continuum that can be approximated by five discrete AO-like pattern, which overlap with the discrete NAO-like pattern. These findings explain why separate NAO regimes are not identified in this analysis.

The negative AO regime is the most distinguishable mode of the QG3 model dynamics (Tab. I): its contribution to the network modularity is substantially greater than the contribution of the other two modes, although with a small frequency of occurrence. For this reason, the most central states of this mode are well separated from other states, with excursions into the area of large negative values of the first leading KPC. Consequently, the transitions to this regime look like rare irregular outliers in the time series of the first KPC (see Fig. 5, bottom). Indeed, this KPC1 can be considered as an index describing joint AO and NAO dynamics. At the same time, the second variable (KPC2) helps differentiate between the positive AO and negative PNA states (Fig.5 top), both of which contribute to the positive NAO.

Let us now turn to the dynamical properties by consider-



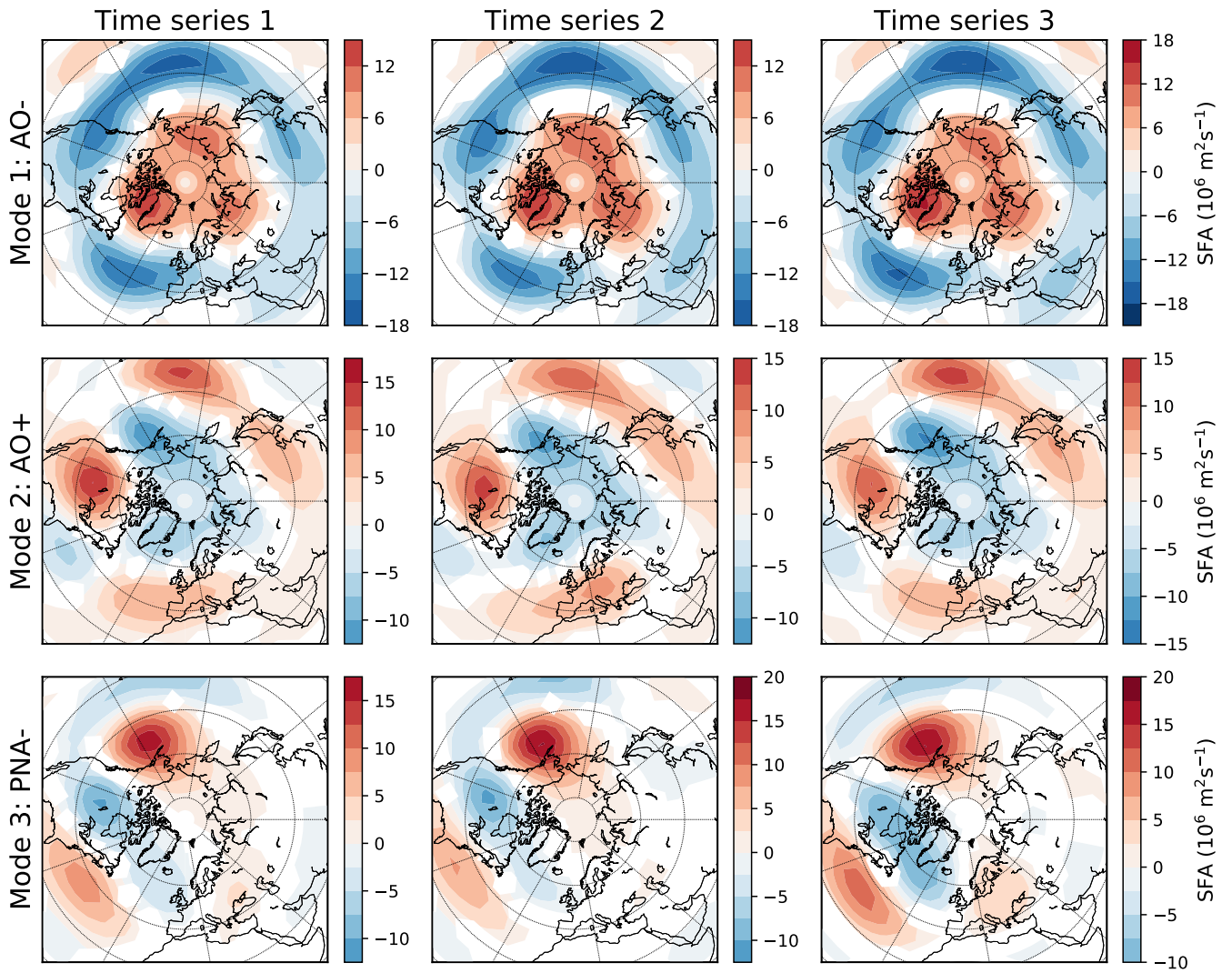


FIG. 6: Composite patterns of the QG3 model SFA corresponding to the obtained regimes. Columns correspond to different time series, rows to different regimes. The composites are calculated as SFA averaged over 20% most typical states of each of the obtained regimes (see the text). Only values that are significantly different from zero by Student's t-test with a critical value of 0.01 are shown.

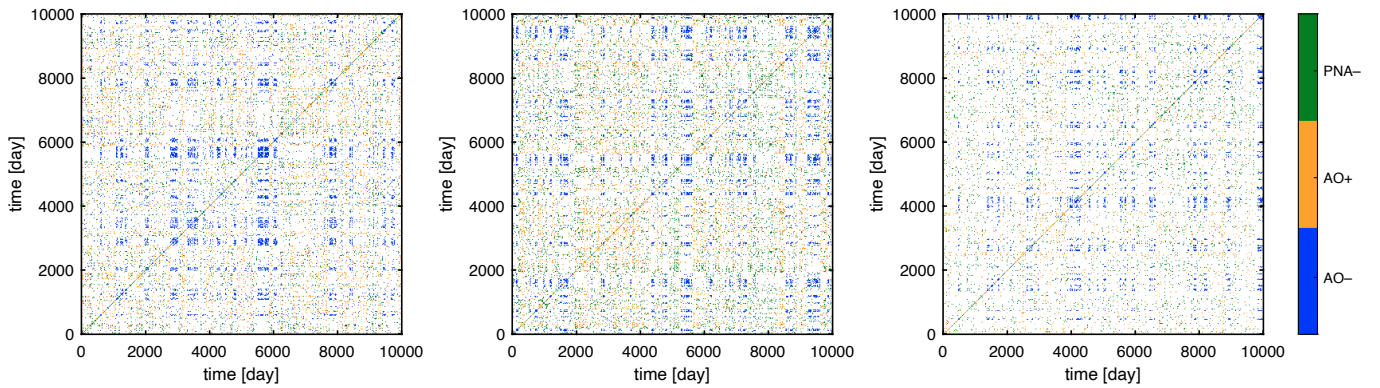


FIG. 7: Recurrence plots of atmospheric patterns obtained from the QG3 model data for the three different time series. Recurrences within a given regime are color coded accordingly. A specific rendering is used to make the RP appear less sparse.

ing the RPs separately for each regime (Fig. 7, see also Sect. II C), along with the RQA (Fig. 8). The RQA reveals

distinct dynamical properties of the identified regimes (Fig. 8 and supplementary Fig. 1). The negative AO regime stands out as the most similar, persistent and predictable regime. This suggests that it encompasses periods of atmospheric blocking as these are characterized by atmospheric patterns that persistently reside for relatively long time periods without significant spatial variations. During a blocking event, atmospheric conditions are consequently more similar and predictable. On the other hand, the negative AO regime is characterised by a high degree of diversity, reflecting the low predictability of blocking events on interannual and decadal time scales. These findings are fostered by the corresponding regime-specific RP (Fig. 7); on longer time scales, the RP appears heterogeneous while block-structures reflect periods of atmospheric blocking. The positive AO regime is associated with stronger westerly zonal flow which appears to result in transient, short-lived atmospheric patterns that do neither exhibit a significant degree of persistence nor allow for reliable short-term predictions. Low-frequency variability of atmospheric patterns in this regime is relatively low as indicated by low values in the different RL measures. Time periods, during which atmospheric conditions are characterized best by the negative PNA regime are identified with moderately predictable and persistent dynamics. Given the total time this regime is detected, the number of recurrences is relatively low, representing low similarity. Both diagonal and vertical line structures in the regime-specific RP exhibit strong heterogeneity, suggesting that the temporal variations in this regime run through both well-predictable, persistent and stochastic, volatile periods. This could be interpreted as a high degree of non-stationarity of the dynamical properties of this regime. Finally, results between the three different time series show good general correspondence (supplementary Fig. 1), supporting the given interpretation of regimes. The most significant deviation is found for the first time series compared to the second and the third with respect to the similarity of all three regimes.

Overall, the results (Figs. 5, 6, Tab. I and supplementary Fig. 1) confirm that the suggested methodology gives a fairly stable solution: the number of regimes, their spatial and temporal structures, the embedding spaces, as well as the modularity rates, show coherency between the three different, independently analyzed time series.

## B. Reanalysis data

For the HGT reanalysis data we detect four regimes (Fig. 9, Tab. II). These communities are embedded well in the space of three leading KPCs, organized into a loop/ring (Fig. 9). The composites form typical HGT patterns in each community (Fig. 10). Additionally, in order to study weather impacts of the detected circulation regimes, we take the same dates as used for the HGT composites to calculate the composites of near-surface air temperature anomalies<sup>48</sup> (Fig. 11).

The composites (Fig. 10) demonstrate qualitatively different structures of atmospheric anomalies related to the detected regimes. The first regime is characterized by anticyclonic anomalies south of Greenland, projecting onto negative AO

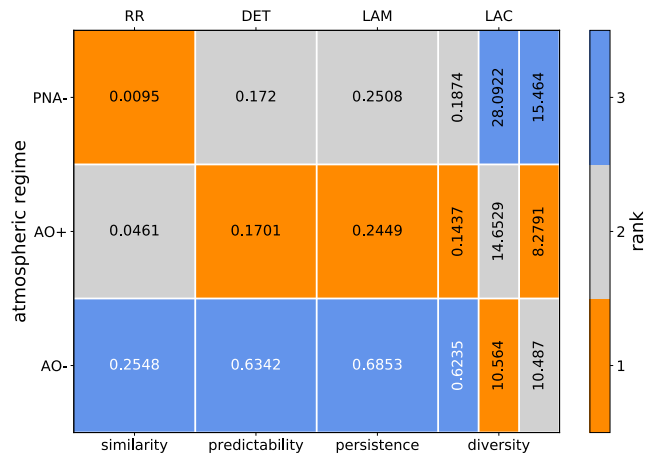


FIG. 8: Results of recurrence quantification analysis for the atmospheric regimes obtained in the QG3 model data set for one of the three time series. The four different RQA measures are labelled with their respective interpretation. Significant (insignificant) values are printed in white (black) numbers. Color coding illustrates the ordering of the RQA values (ascending column-ranking) for better comparability.

and NAO. This pattern blocks the transport of warm air from the Atlantic to Europe, while increasing the advection of subtropical air to the northeast of North America, and advecting warm/humid air into North Africa (Fig. 11). The second regime features a positive NAO and PNA<sup>3,4</sup>, manifested by a lowering pressure over the North Atlantic and increasing pressure in the northeastern Pacific Ocean. Anticyclonic anomalies in the Pacific Ocean block zonal airflow and lead to cooling in northern USA and Canada and warming in eastern Russia and Arctic. The third regime with a high pressure center over northwest Russia and Scandinavia slows down zonal air transport in the Euro-Atlantic region, leading to extremely cold winters in Europe and heating the Arctic Ocean area north of central Russia. Simultaneously, stable zonal flow over the north Pacific induces warm conditions in Canada (Fig. 11). Finally, the fourth flow pattern relates to positive AO and NAO<sup>39,45</sup>; it is characterized by increased zonal airflow in the north Atlantic, providing warmer than normal winters in Europe and Russia (Fig. 11).

The number of days in each winter corresponding to a given flow regime (Fig. 9), as well as in the KPC time series (not shown), we observe pronounced strong inter-annual variability of dominating types of behavior of the winter atmospheric circulation. In particular, we see that regimes 1 and 3, leading to cold weather in Europe, can be correlated on a large scale. The amplitude of the inter-annual variability is not regular; e.g., there are sets of extreme winters with strong domination of a single regime (see, for example, the abnormal winters 2009-10 and 2019-20 showing domination of regimes 1 and 4, respectively). Regimes 1 and 2 occur less often than 3 and 4 (Fig. 9, Tab. II), although they have larger modularity per state, i.e., the HGT states belonging to them are more distinguishable.

|  | Community 1 (AO-)   | Community 2 (AO+)   | Community 3 (PNA-)  |
|--|---------------------|---------------------|---------------------|
| Modularity (TS1; TS2; TS3)                                 | 0.219; 0.222; 0.228 | 0.169; 0.174; 0.155 | 0.107; 0.118; 0.103 |
| Number of states (TS1; TS2; TS3)                           | 2235; 1861; 2484    | 3746; 3863; 4058    | 4019; 4275; 3458    |
| Modularity per state (TS1, TS2, TS3), ( $\times 10^{-5}$ ) | 9.8; 11.9; 9.18     | 4.51; 4.5; 3.82     | 2.66; 2.76; 2.98    |

TABLE I: Parameters of the communities extracted from three analyzed time series of the QG3 model (the time series are referred to as TS1, TS2 and TS3). First row: contribution of a community to the network modularity. Second row: the number of SFA states (number of days) belonging to a community. Third row: mean contribution of a state to the modularity of its community.

Atmospheric patterns characteristic for the first regime are rendered persistent and predictable at intra-seasonal time scales (Fig.12). However, this regime exhibits high diversity, indicating strong variability at longer (inter-annual and decadal) time scales. This corroborates the general finding that atmospheric blocking structures entail stationary winter atmospheric circulation while their prediction at inter-annual to decadal time scales is cumbersome. We find significantly high similarity for the second regime, implying that the spatial anticyclonic anomaly patterns characteristic for this regime are comparable between different years. Note that high similarity obtained for the first and second regimes is likely the source of large values of the modularity per state within these regimes (see Tab. II). Conversely, we find that atmospheric conditions as identified in the third regime which, e.g., often result in extremely cold European winters are poorly predictable at intra-seasonal time scales. Finally, positive AO and NAO phases as represented by the fourth regime are dynamically opposite to the atmospheric blocking structures (negative AO and NAO) captured by the first regime.

This is in agreement with Woollings et al.<sup>12</sup>, and references therein, who investigated the NAO time scales. They found that the two phases of the NAO have intrinsically different decay characteristics, with the negative NAO events showing enhanced persistence associated with blocking, see also Ref. 49. Woollings et al.<sup>13</sup> investigate the jet positions over the North Atlantic region. They found that the southern jet position, associated with the negative NAO phase (and Greenland blocking) has smaller tendency, and therefore more persistent (see Ref. 3) than the northern position, associated with the positive NAO phase.

## V. SUMMARY AND CONCLUSIONS

The proposed method allows us to (1) reveal recurrent regimes of atmospheric circulation from spatially distributed observations, and, simultaneously, (2) obtain a set of dynamical variables serving as an embedding for the regimes. A combination of the two nonlinear data-driven approaches – KPCA and recurrence analysis – provides comprehensive investigation of the mode content of the observed dynamics, including the regime identification, their dynamical representation and characteristics, and analyzing the dynamical properties of inter-regime evolution. Both parts of the method are based on constructing the same kernel matrix that consists of pairwise similarities between atmospheric states at different

dates. In the first part this matrix produces the recurrence network, which when partitioned yields separation of all observed states into the regimes. RQA applied to the obtained submatrices relating to different regimes (or communities), helps to study important properties of temporal evolution of the regimes, e.g., predictability, persistence, similarity, and intermittency. In the second part, the principal components of the kernel matrix (KPCs) are used to construct a space in which the states belonging to different regimes are well-separated.

It is worth noting that the KPCA with Gaussian kernels is very close to the diffusion map method<sup>50</sup>, based on decomposition of a diffusion operator reconstructed from the data. More precisely, the 1-step diffusion maps should give the same, up to a transformation, basis of principal components as Gaussian KPCA. Thus, we can expect a clear separation of the regimes in the diffusion space too. Moreover, probably the use of n-step diffusion map space as an embedding for the regimes may be more effective, since it is more robust to noise due to many paths between network’s nodes being involved. In this work we demonstrate that even the basic Gaussian KPCA represents well the recurrence network communities due to the same distance matrix used in both the RP and Gaussian kernels. In future the diffusion maps can be adopted for this purpose.

We demonstrate, using both model and observation data, that the detected regimes of the Northern Hemisphere mid-latitude winter atmosphere correspond to qualitatively different states, which cover the well-known modes NAO, AO, and PNA. We show that typically only a few leading KPCs are sufficient for the embedding of the regimes. Thus, these KPCs can be used as dynamical variables describing the alternation of the obtained regimes, and future works can aim at predictive data-driven models of their dynamics (see, e.g., Refs. 51 and 52). Moreover, having the dynamical variables representing the atmospheric modes, we can state a problem of finding long-term climatic predictors (e.g., ENSO, QBO, solar cycle, etc.) making it possible to elaborate a scheme for inter-annual forecast of dominating weather patterns.

The kernels Eq. (4), based on the distance Eq.(8), reflect similarity between two short-term patterns, each realized within one day. This leads to extracting the recurrent but not necessary persistent patterns (the persistence is separately studied by the RQA), which are distributed over the whole mid-latitude belt. However, we can change the distance definition, adapting it to the desired properties of regimes to extract. For example, we can target the method to long-living

|   | Community 1 | Community 2 | Community 3 | Community 4 |
|---|-------------|-------------|-------------|-------------|
| Modularity                                | 0.109       | 0.122       | 0.115       | 0.13        |
| Number of states                          | 777         | 890         | 940         | 1062        |
| Modularity per state, ( $\cdot 10^{-4}$ ) | 1.4         | 1.37        | 1.22        | 1.22        |

TABLE II: The same as in Table I, but for the regimes obtained from the reanalysis HGT data set.

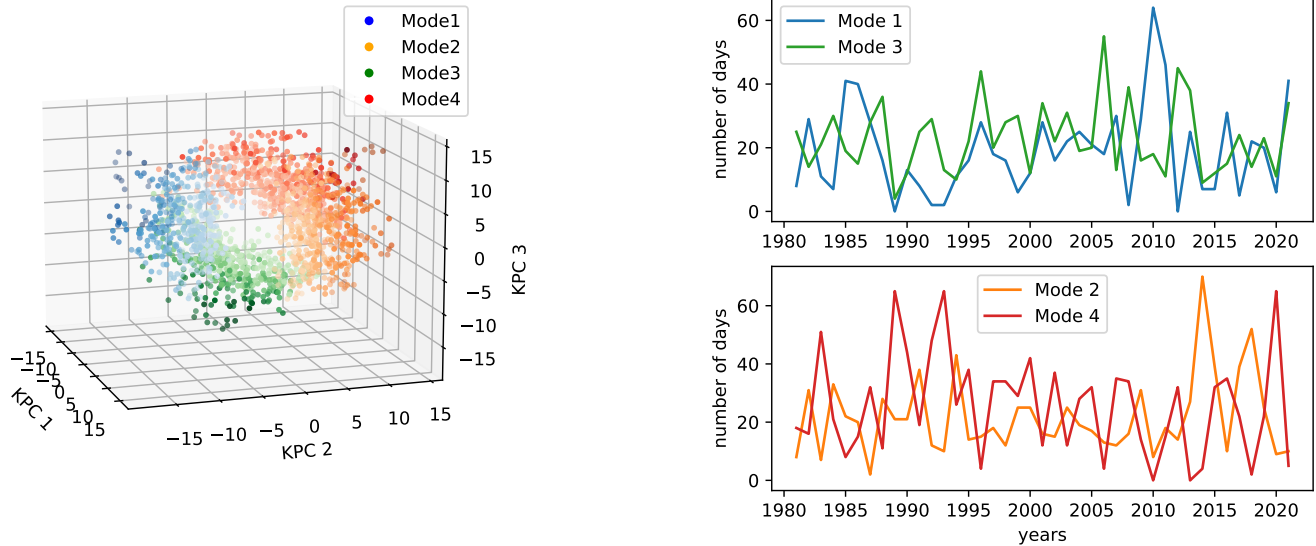


FIG. 9: Partitioning of HGT states into regimes. Left panel: 50% of the most typical states of each regime (mode) in the space of three leading KPCs. Color saturation corresponds to the centrality value of a state in its community. Right panel: number of days per winter related to different regimes. The years of January of each winter are shown (e.g., 2001 corresponds to the winter 2000-2001).

(persistent) regimes via time-lag extension of states, or use other weightings, Eq. (9), to emphasize some geographical regions. Those topics are left for future research.

<sup>1</sup> A. Hannachi, *Patterns Identification and Data Mining in Weather and Climate* (Springer, Cham, 2021).

<sup>2</sup> P. Sura and A. Hannachi, “Perspectives of non-gaussianity in atmospheric synoptic and low-frequency variability,” *Journal of Climate* **28**, 5091 – 5114 (2015).

<sup>3</sup> A. Hannachi, D. M. Straus, C. L. E. Franzke, S. Corti, and T. Woollings, “Low-frequency nonlinearity and regime behavior in the northern hemisphere extratropical atmosphere,” *Reviews of Geophysics* **55**, 199–234 (2017), <https://agupubs.onlinelibrary.wiley.com/doi/pdf/10.1002/2015RG000509>.

<sup>4</sup> J. M. Wallace and D. S. Gutzler, “Teleconnections in the geopotential height field during the northern hemisphere winter,” *Monthly Weather Review* **109**, 784 – 812 (1981).

<sup>5</sup> A. G. Barnston and R. E. Livezey, “Classification, seasonality and persistence of low-frequency atmospheric circulation patterns,” *Monthly Weather Review* **115**, 1083 – 1126 (1987).

<sup>6</sup> C. Cassou, “Intraseasonal interaction between the madden–julian oscillation and the north atlantic oscillation,” *Nature* **455**, 523–527 (2008).

<sup>7</sup> M. Ghil and A. W. Robertson, ““waves” vs. “particles” in the atmosphere’s phase space: A pathway to long-range forecasting?” *Proceedings of the National Academy of Sciences* **99**, 2493–2500 (2002), <https://www.pnas.org/doi/pdf/10.1073/pnas.012580899>.

<sup>8</sup> C. Franzke and S. B. Feldstein, “The continuum and dynamics of northern hemisphere teleconnection patterns,” *Journal of the Atmospheric Sciences* **62**, 3250–3267 (2005).

<sup>9</sup> S. J. Colucci and D. P. Baumhefner, “Initial weather regimes as predictors

of numerical 30-day mean forecast accuracy,” *Journal of Atmospheric Sciences* **49**, 1652 – 1671 (1992).

<sup>10</sup> R. M. Dole, “Persistent anomalies of the extratropical northern hemisphere wintertime circulation: Structure,” *Monthly Weather Review* **114**, 178 – 207 (1986).

<sup>11</sup> L. Pandolfo, “Observational aspects of the low-frequency intraseasonal variability of the atmosphere in middle latitudes,” (Elsevier, 1993) pp. 93–174.

<sup>12</sup> T. Woollings, A. Hannachi, B. Hoskins, and A. Turner, “A regime view of the north atlantic oscillation and its response to anthropogenic forcing,” *Journal of Climate* **23**, 1291 – 1307 (2010).

<sup>13</sup> T. Woollings, A. Hannachi, and B. Hoskins, “Variability of the north atlantic eddy-driven jet stream,” *Quarterly Journal of the Royal Meteorological Society* **136**, 856–868 (2010), <https://rmets.onlinelibrary.wiley.com/doi/pdf/10.1002/qj.625>.

<sup>14</sup> A. Hannachi and W. Iqbal, “Bimodality of hemispheric winter atmospheric variability via average flow tendencies and kernel eofs,” *Tellus A: Dynamic Meteorology and Oceanography* **71**, 1633847 (2019), <https://doi.org/10.1080/16000870.2019.1633847>.

<sup>15</sup> A. Hannachi and W. Iqbal, “On the Nonlinearity of Winter Northern Hemisphere Atmospheric Variability,” *Journal of the Atmospheric Sciences* **76**, 333–356 (2019).

<sup>16</sup> Y. Zou, R. V. Donner, N. Marwan, J. F. Donges, and J. Kurths, “Complex network approaches to nonlinear time series analysis,” *Physics Reports* **787**, 1–97 (2019).

<sup>17</sup> J. B. Tenenbaum, V. de Silva, and J. C. Langford, “A global geometric framework for nonlinear dimensionality reduction,” *Science* **290**, 2319–2323 (2000), <https://www.science.org/doi/pdf/10.1126/science.290.5500.2319>.

<sup>18</sup> A. Hannachi and A. G. Turner, “20th century intraseasonal asian monsoon dynamics viewed from isomap,” *Nonlinear Processes in Geophysics* **20**,



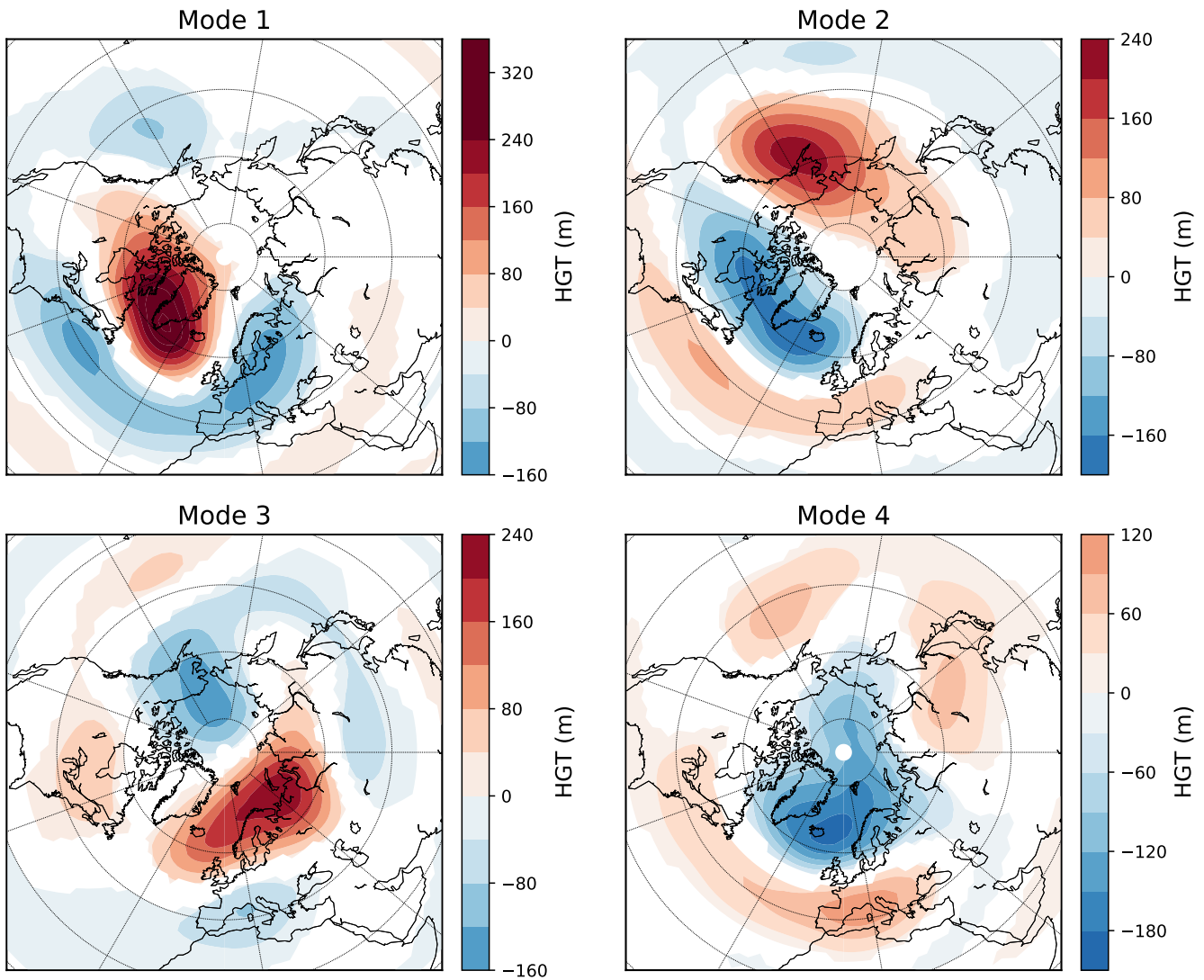


FIG. 10: Composite patterns of HGT corresponding to the obtained regimes. The composites are calculated as HGT averaged over 20% most typical states of each of the regimes. Only values that are significantly different from zero by Student's t-test with a critical value of 0.01 are shown.

725–741 (2013).

<sup>19</sup>M. E. J. Newman, “Modularity and community structure in networks,” *Proceedings of the National Academy of Sciences* **103**, 8577–8582 (2006), <https://www.pnas.org/content/103/23/8577.full.pdf>.

<sup>20</sup>N. Marwan, J. F. Donges, Y. Zou, R. V. Donner, and J. Kurths, “Complex network approach for recurrence analysis of time series,” *Physics Letters A* **373**, 4246–4254 (2009).

<sup>21</sup>N. Marwan, M. Carmen Romano, M. Thiel, and J. Kurths, “Recurrence plots for the analysis of complex systems,” *Physics Reports* **438**, 237–329 (2007).

<sup>22</sup>B. Schölkopf, A. Smola, and K.-R. Müller, “Nonlinear Component Analysis as a Kernel Eigenvalue Problem,” *Neural Computation* **10**, 1299–1319 (1998), <https://direct.mit.edu/neco/article-pdf/10/5/1299/813905/089976698300017467.pdf>.

<sup>23</sup>B. E. Boser, I. M. Guyon, and V. N. Vapnik, “A training algorithm for optimal margin classifiers,” in *Proceedings of the Fifth Annual Workshop on Computational Learning Theory, COLT ’92* (Association for Computing Machinery, New York, NY, USA, 1992) p. 144–152.

<sup>24</sup>J. Schoenberg, “Metric spaces and positive definite functions,” *Transac-*

*tions of the American Mathematical Society* **44**, 522–522 (1938).

<sup>25</sup>This situation is out of scope in this article.

<sup>26</sup>D. Reynolds, “Gaussian mixture models,” in *Encyclopedia of Biometrics*, edited by S. Z. Li and A. Jain (Springer US, Boston, MA, 2009) pp. 659–663.

<sup>27</sup>B. W. Silverman, *Density Estimation for Statistics and Data Analysis* (Chapman & Hall, London, 1986).

<sup>28</sup>M. E. J. Newman and M. Girvan, “Finding and evaluating community structure in networks,” *Phys. Rev. E* **69**, 026113 (2004).

<sup>29</sup>In practice, however, we may consider using a threshold slightly above zero to avoid “too thin” separation, if, for example, further splitting gives much less modularity increment as compared with the previous splits.

<sup>30</sup>T. Braun, V. R. Unni, R. Sujith, J. Kurths, and N. Marwan, “Detection of dynamical regime transitions with lacunarity as a multiscale recurrence quantification measure,” *Nonlinear Dynamics*, 1–19 (2021).

<sup>31</sup>N. Marwan, S. Schinkel, and J. Kurths, “Recurrence plots 25 years later—gaining confidence in dynamical transitions,” *EPL (Europhysics Letters)* **101**, 20007 (2013).

<sup>32</sup>J. Marshall and F. Molteni, “Toward a dynamical understand-



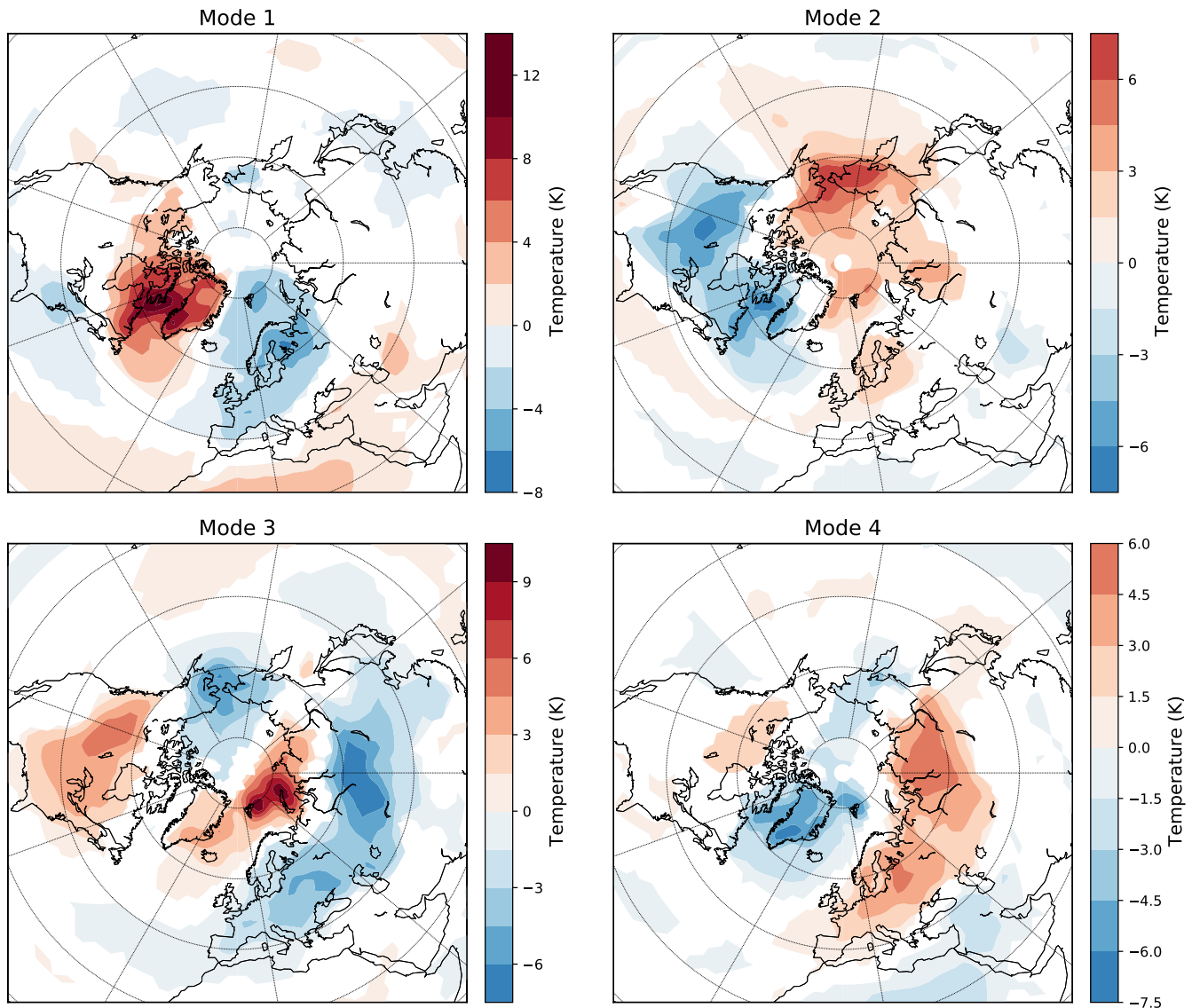


FIG. 11: Composite patterns of surface air temperatures (SAT) corresponding to the obtained HGT regimes. The composites are calculated as SAT averaged over 20% most typical states of each of the regimes. Only values that are significantly different from zero by Student's t-test with a critical value of 0.01 are shown.

ing of planetary-scale flow regimes," *Journal of the Atmospheric Sciences* **50**, 1792–1818 (1993), [https://doi.org/10.1175/1520-0469\(1993\)050<1792:TADUOP>2.0.CO;2](https://doi.org/10.1175/1520-0469(1993)050<1792:TADUOP>2.0.CO;2).

<sup>33</sup>S. Vannitsem and C. Nicolis, "Lyapunov vectors and error growth patterns in a t2113 quasigeostrophic model," *Journal of the Atmospheric Sciences* **54**, 347–361 (1997), [https://doi.org/10.1175/1520-0469\(1997\)054<0347:LVAEGP>2.0.CO;2](https://doi.org/10.1175/1520-0469(1997)054<0347:LVAEGP>2.0.CO;2).

<sup>34</sup>S. Corti, A. Giannini, S. Tibaldi, and F. Molteni, "Patterns of low-frequency variability in a three-level quasi-geostrophic model," *Climate Dynamics* **13**, 883–904 (1997).

<sup>35</sup>D. Kondrashov, K. Ide, and M. Ghil, "Weather regimes and preferred transition paths in a three-level quasigeostrophic model," *Journal of the Atmospheric Sciences* **61**, 568–587 (2004), [https://doi.org/10.1175/1520-0469\(2004\)061<0568:WRAPTP>2.0.CO;2](https://doi.org/10.1175/1520-0469(2004)061<0568:WRAPTP>2.0.CO;2).

<sup>36</sup>A. Seleznev, D. Mukhin, A. Gavrilov, E. Loskutov, and A. Feigin, "Bayesian framework for simulation of dynamical systems from multi-dimensional data using recurrent neural network," *Chaos: An Interdisciplinary Journal of Nonlinear Science* **29**, 123115 (2019).

<sup>37</sup>E. Kalnay, M. Kanamitsu, R. Kistler, W. Collins, D. Deaven, L. Gandin, M. Iredell, S. Saha, G. White, J. Woollen, Y. Zhu, A. Leetmaa, R. Reynolds, M. Chelliah, W. Ebisuzaki, W. Higgins, J. Janowiak, K. C. Mo, C. Ropelewski, J. Wang, R. Jenne, and D. Joseph, "The NCEP/NCAR 40-year reanalysis project," *Bulletin of the American Meteorological Society* **77**, 437–471 (1996).

<sup>38</sup>N. Marwan, "How to avoid potential pitfalls in recurrence plot based data analysis," *International Journal of Bifurcation and Chaos* **21**, 1003–1017 (2011).

<sup>39</sup>D. W. J. Thompson and J. M. Wallace, "The arctic oscillation signature in the wintertime geopotential height and temperature fields," *Geophysical Research Letters* **25**, 1297–1300 (1998), <https://agupubs.onlinelibrary.wiley.com/doi/pdf/10.1029/98GL00950>.

<sup>40</sup>K. Haines and A. Hannachi, "Weather regimes in the pacific from a gcm," *Journal of Atmospheric Sciences* **52**, 2444 – 2462 (1995).

<sup>41</sup>A. Hannachi, "Low-frequency variability in a gcm: Three-dimensional flow regimes and their dynamics," *Journal of Climate* **10**, 1357 – 1379 (1997).

<sup>42</sup>J. Pedlosky, *Geophysical Fluid Dynamics* (Springer New York, 1987).

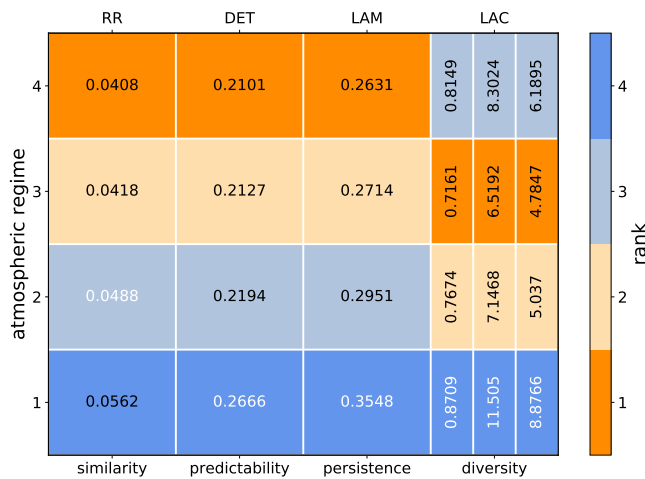


FIG. 12: Results of recurrence quantification analysis for the atmospheric regimes obtained in the reanalysis data set. The four different RQA measures are labelled with their respective interpretation. Values that significantly exceed the values corresponding to randomly obtained partitions (see the text) are printed in white; other values are printed in black. Color coding illustrates the ordering of the RQA values (ascending column-ranking) for better comparability.

- <sup>43</sup>D. Mukhin, A. Gavrillov, A. Feigin, E. Loskutov, and J. Kurths, “Principal nonlinear dynamical modes of climate variability,” *Scientific Reports* **5**, 15510 (2015).
- <sup>44</sup>D. Mukhin, A. Gavrillov, E. Loskutov, A. Feigin, and J. Kurths, “Nonlinear reconstruction of global climate leading modes on decadal scales,” *Climate Dynamics* **51**, 2301–2310 (2018).
- <sup>45</sup>J. M. Wallace, “North atlantic oscillation/annular mode: Two paradigms—one phenomenon,” *Quarterly Journal of the Royal Meteorological Society* **126**, 791–805 (2000), <https://rmets.onlinelibrary.wiley.com/doi/pdf/10.1002/qj.49712656402>.
- <sup>46</sup>S. B. Feldstein and C. Franzke, “Are the north atlantic oscillation and the northern annular mode distinguishable?” *Journal of the Atmospheric Sciences* **63**, 2915 – 2930 (2006).
- <sup>47</sup>P. Dai and B. Tan, “The nature of the arctic oscillation and diversity of the extreme surface weather anomalies it generates,” *Journal of Climate* **30**, 5563 – 5584 (2017).
- <sup>48</sup>We use air temperature data at 0.995 sigma level taken from the NCEP/NCAR reanalysis<sup>37</sup>. The anomalies were produced by deseasonalizing in the same way as with the HGT data (see Sec. III.III B).
- <sup>49</sup>T. Onskog, C. Franzke, and A. Hannachi, “Nonlinear time series models for the north atlantic oscillation,” *Advances in Statistical Climatology, Meteorology and Oceanography* **6**, 141–157 (2020).
- <sup>50</sup>R. R. Coifman and S. Lafon, “Diffusion maps,” *Applied and Computational Harmonic Analysis* **21**, 5–30 (2006), special Issue: Diffusion Maps and Wavelets.
- <sup>51</sup>A. Gavrillov, A. Seleznev, D. Mukhin, E. Loskutov, A. Feigin, and J. Kurths, “Linear dynamical modes as new variables for data-driven ENSO forecast,” *Climate Dynamics* **52**, 2199–2216 (2019).
- <sup>52</sup>D. Mukhin, A. Gavrillov, E. Loskutov, J. Kurths, and A. Feigin, “Bayesian Data Analysis for Revealing Causes of the Middle Pleistocene Transition,” *Scientific Reports* **9** (2019), 10.1038/s41598-019-43867-3.
- <sup>53</sup>A. Hannachi and A. O’Neill, “Atmospheric multiple equilibria and non-gaussian behaviour in model simulations,” *Quarterly Journal of the Royal Meteorological Society* **127**, 939–958 (2001), <https://rmets.onlinelibrary.wiley.com/doi/pdf/10.1002/qj.49712757312>.
- <sup>54</sup>S. Kravtsov, D. Kondrashov, and M. Ghil, “Multilevel regression modeling of nonlinear processes: Derivation and applications to climatic variability,” *Journal of Climate* **18**, 4404 – 4424 (2005).

## SUPPLEMENTARY MATERIAL

See the supplementary material that includes supplementary figures 1 and 2.

## ACKNOWLEDGMENTS

The authors are grateful to the two anonymous reviewers for fruitful suggestions and comments. They helped to improve the article significantly. The QG3 model code is provided by the courtesy of Dmitri Kondrashov (UCLA) and Fabio d’Andrea (ENS). This work was supported by the grant #22-12-00388 of the Russian Science Foundation (D. Mukhin) and Deutsche Forschungsgemeinschaft in the context of the DFG project MA4759/11-1 ‘Nonlinear empirical mode analysis of complex systems: Development of general approach and application in climate’ (T. Braun).

## AUTHOR DECLARATION

### Conflict of Interest

The authors have no conflicts to disclose.

### Author Contributions

DM and AH developed the method for detecting regimes, TB and NM analyzed the regimes by the RQA approach. All the authors analyzed results and contributed to writing the manuscript.

## DATA AVAILABILITY STATEMENT

The data that support the findings of this study are openly available in NCEP/NCAR reanalysis<sup>37</sup> archive at <https://psl.noaa.gov/data/gridded/data.ncep.reanalysis.html>. The time series of the QG3 model are available upon request.

## Appendix A: Simple model example

This section demonstrates the ability of the proposed method to detect and separate recurrent states in a simple situation, when the true solution is known. We use a toy two-dimensional stochastic model with three-well potential, which was suggested in the work 53 for testing a clustering method and then also used in the work 54:

$$d\mathbf{X} = -\nabla V(\mathbf{X}) + \varepsilon dW_t$$

$$V(\mathbf{X}) = u(\mathbf{X} - \mathbf{A}_1) + u(\mathbf{X} - \mathbf{A}_2) + u(\mathbf{X} - \mathbf{A}_3) + b|\mathbf{X} - \mathbf{A}_c|^2,$$

(A1)

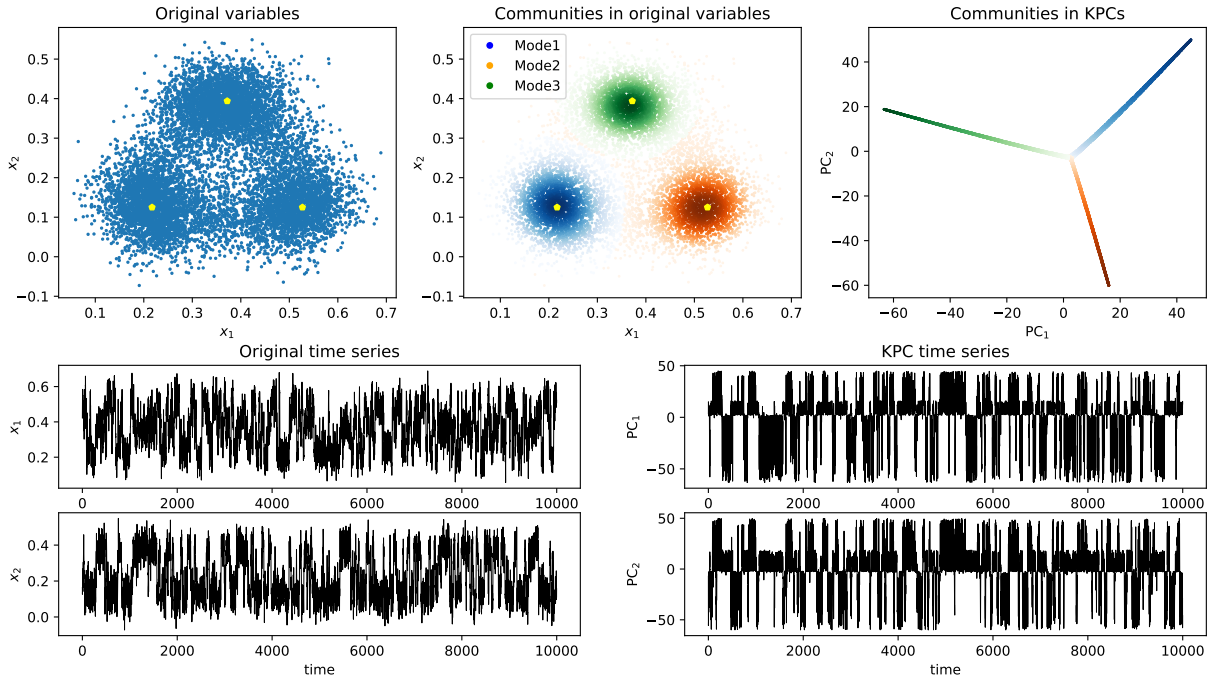


FIG. 13: Analysis of time series of the three-well model (Eq. A1-A2) based on the simple Euclidean distance between state vectors. Upper panels (from left to right): analyzed time series presented in original variables; the same, but with states marked according with the regimes they belong to; analyzed time series presented on the plain of leading two KPCs. Yellow dots mark “theoretical” centers of the potential function  $V(\cdot)$ . Color intensity corresponds to centrality of a state in its community. Low panels: time series of original variables (left) and leading two KPCs (right).

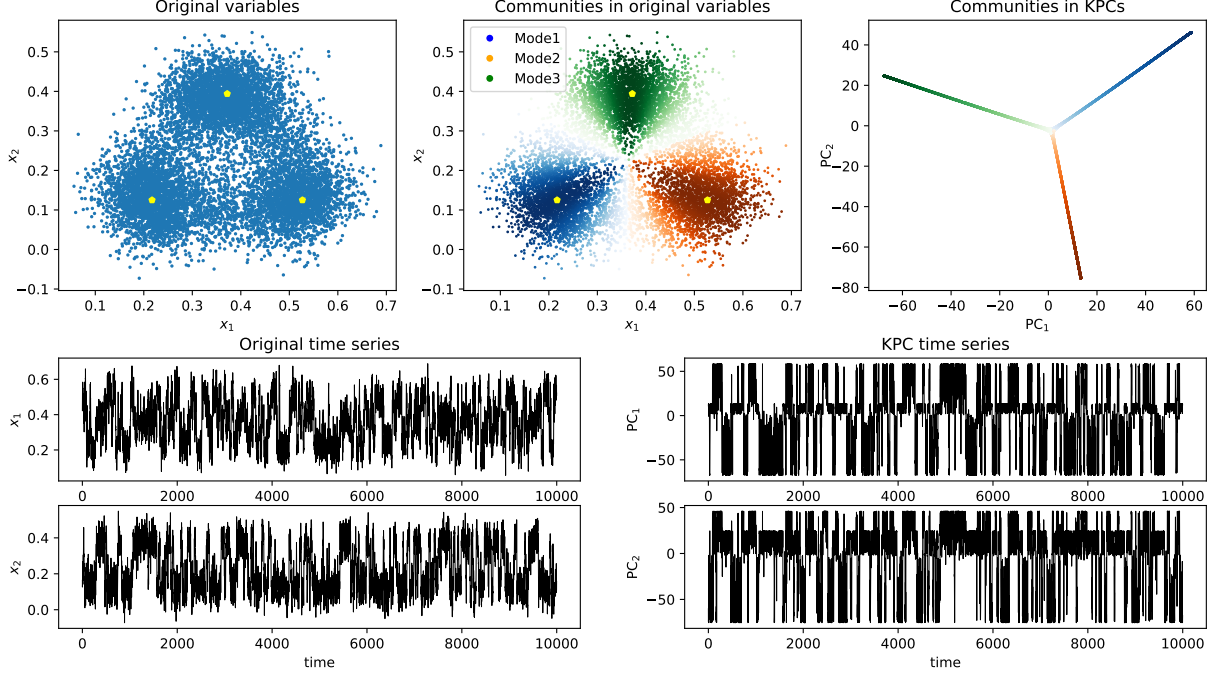


FIG. 14: The same analysis as in Fig. 13, but based on Euclidean distance between normalized vectors defined by Eq. 8.

where  $W_t$  is the Wiener process, points  $A_1 = (0, 0)$ ,  $A_2 = (2a, 0)$  and  $A_3 = (a, a\sqrt{3})$  are the centers of profiles  $u(\cdot)$  which

takes the form

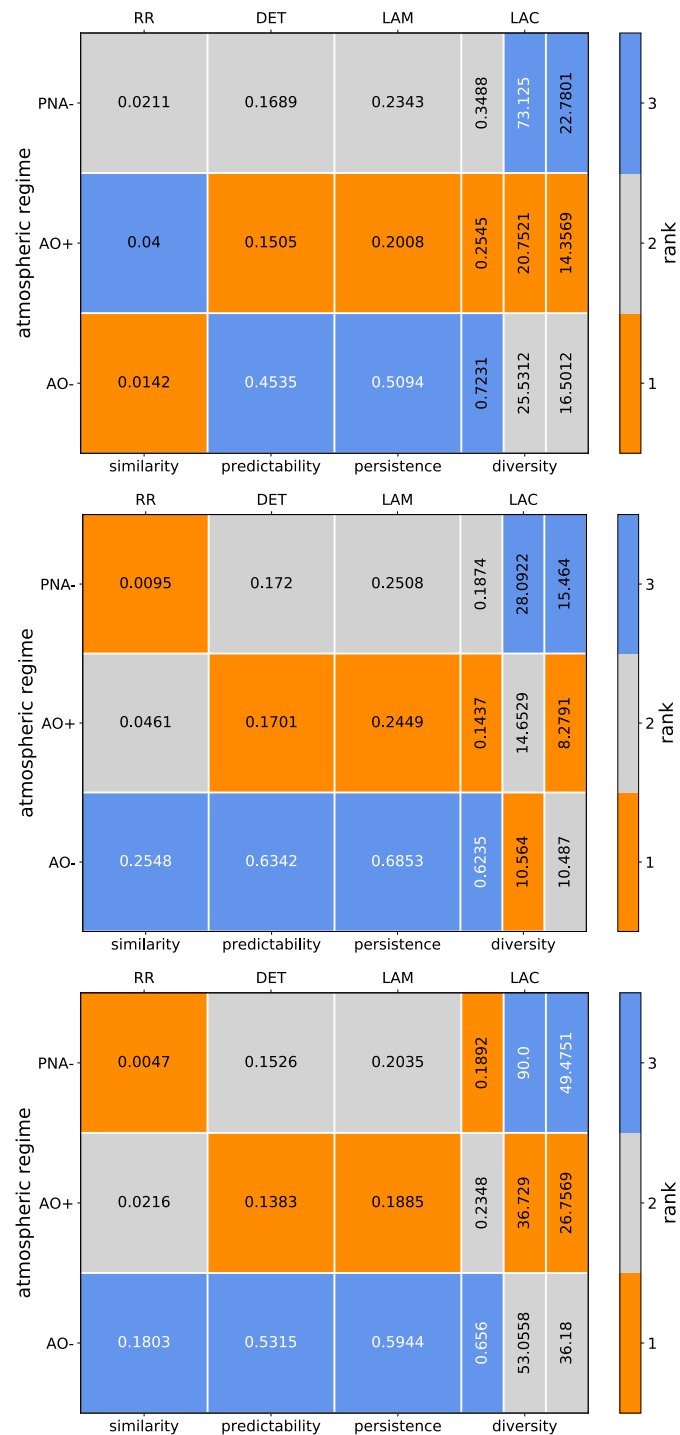
$$u(\mathbf{X}) = -\alpha \exp \left[ \frac{1}{|\mathbf{X}|^2 - a^2} \right]. \quad (\text{A2})$$

The potential function  $V(\mathbf{X})$  has three minima placed in the vertices of a isosceles triangle centered in  $A_c = \left(a, \frac{a}{\sqrt{3}}\right)$ . Here we use the same values of parameters as in Ref. 53:  $\alpha = 21$ ,  $a = 0,87$ ,  $b = 0,12$  and  $\varepsilon = 0.05$ . This model produces random walks around the local minima of the potential function, provided that the phase trajectory spends more time near the centers of the potential than anywhere else. Thereby, the model simulates the situation with three regimes, or recurrent states in the phase space.

We integrate this model by Euler method with the time step 0.01. To exclude from consideration the points which are close to each other due to the temporal ordering, we take only each 100th point during the integration. For analysis we use 10,000-point time series (Fig. 13 and 14) taken after 20,000-step spin-up period.

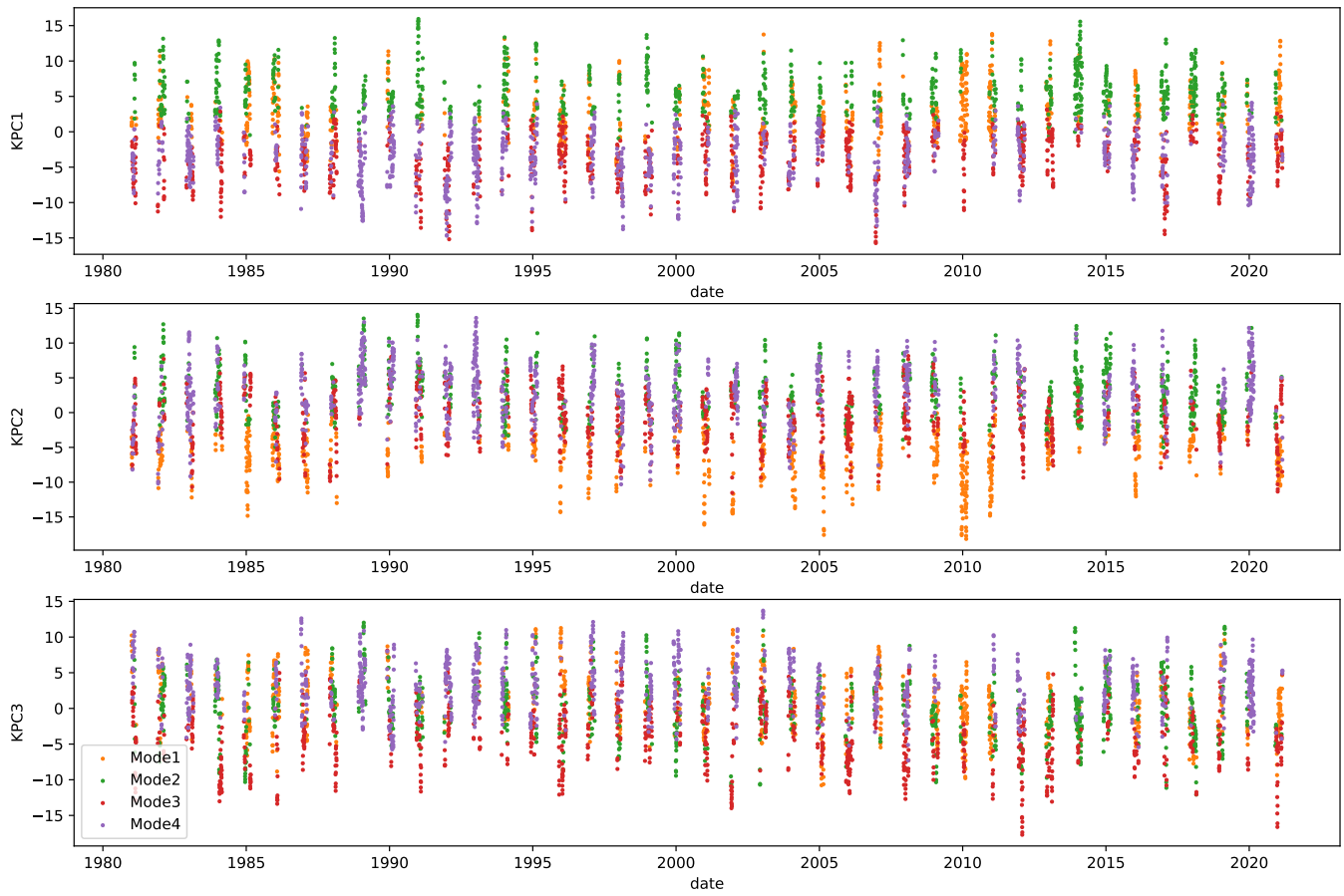
We applied the presented method to this data, based on two different distances: (i) simple Euclidean distance  $d_{ij} =$

$|\mathbf{X}_i - \mathbf{X}_j|$  and (ii) Euclidean distance between normalized vectors given by Eq. 8. In both cases we detect three regimes, central points of which are separated well in the plane of leading two KPCs (see Fig. 13 and 14). In the projections of the phase trajectory to this plane, states that belong to different regimes fall on different linear manifolds. At the same time, the time series of KPCs describe transitions between areas of the regimes. However, distribution of the centralities substantially depends on the distance choice: if in the first case it emphasizes the maxima of the probability density in 2d-space, in the second case it captures rather the density of angles of centered states vectors, because the normalization in Eq. 8 attaches all vectors to the unit sphere. The latter is especially important in climate applications above, where we are interested in capturing the shapes of spatial patterns rather than their amplitudes.

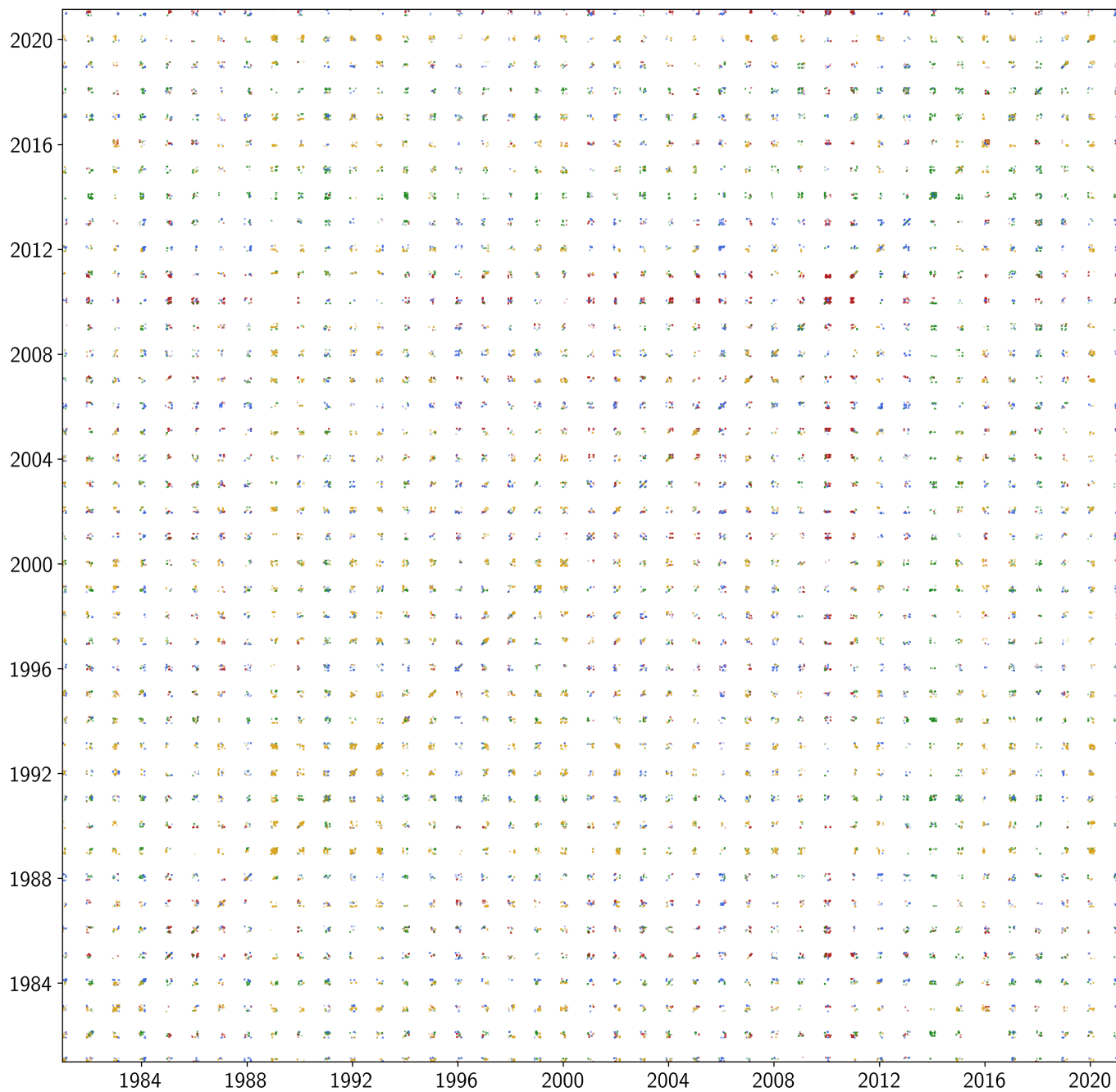


**SUPPL. FIG. 1.** Comparison of results of recurrence quantification analysis for the atmospheric regimes obtained in the QG3 model data set between the three different time series. The four different RQA measures are labelled with their respective interpretation. Significant (insignificant) values are printed in white (black). Color coding illustrates the ordering of the RQA values (ascending column-ranking) for better comparability.





**SUPPL. FIG. 2.** Time series of the leading three KPCs of the reanalysis data. Different colors correspond to the obtained regimes. Since only the winter months are considered, the time series are split into segments separated by equidistant gaps.



**SUPPL. FIG. 3.** Recurrence plot of atmospheric patterns obtained from the reanalysis data. Recurrences within a given regime are color coded accordingly. Since only the winter months are considered, the RP is split into sub-RPs separated by equidistant gaps.